

Multi-Resolution Subspace-Based Optimization Method for the Retrieval of 2D Perfect Electric Conductors

X. Ye,⁽¹⁾ F. Zardi,⁽²⁾⁽³⁾ M. Salucci,⁽²⁾⁽³⁾ and A. Massa,⁽²⁾⁽³⁾⁽⁴⁾⁽⁵⁾

⁽¹⁾ *Beijing Institute of Technology*

School of Information and Electronics, Beijing 1008 - China

E-mail: *xiuzhuye@outlook.com*

⁽²⁾ *ELEDIA Research Center (ELEDIA@UniTN - University of Trento)*

DICAM - Department of Civil, Environmental, and Mechanical Engineering

Via Mesiano 77, 38123 Trento - Italy

E-mail: *{francesco.zardi, marco.salucci, andrea.massa}@unitn.it*

Website: *www.eledia.org/eledia-unitn*

⁽³⁾ *CNIT - "University of Trento" ELEDIA Research Unit*

Via Sommarive 9, 38123 Trento - Italy

Website: *www.eledia.org/eledia-unitn*

⁽⁴⁾ *ELEDIA Research Center (ELEDIA@UESTC - UESTC)*

School of Electronic Engineering, Chengdu 611731 - China

E-mail: *andrea.massa@uestc.edu.cn*

Website: *www.eledia.org/eledia-uestc*

⁽⁵⁾ *ELEDIA Research Center (ELEDIA@TSINGHUA - Tsinghua University)*

30 Shuangqing Rd, 100084 Haidian, Beijing - China

E-mail: *andrea.massa@tsinghua.edu.cn*

Website: *www.eledia.org/eledia-tsinghua*

This work has been submitted to the IEEE for possible publication. Copyright may be transferred without notice, after which this version may no longer be accessible.

Multi-Resolution Subspace-Based Optimization Method for the Retrieval of 2D Perfect Electric Conductors

X. Ye, F. Zardi, M. Salucci, and A. Massa

Abstract

Perfect Electric Conductors (*PECs*) are imaged integrating the subspace-based optimization method (*SOM*) within the iterative multi-scaling scheme (*IMSA*). Without *a-priori* information on the number or/and the locations of the scatterers and modelling their *EM* scattering interactions with a (known) probing source in terms of surface electric field integral equations, a segment-based representation of *PECs* is retrieved from the scattered field samples. The proposed *IMSA-SOM* inversion method is validated against both synthetic and experimental data by assessing the reconstruction accuracy, the robustness to the noise, and the computational efficiency with some comparisons, as well.

Key words: Inverse Problems; Inverse Scattering; Microwave Imaging; Iterative Multi-Scaling Approach; Multi-Resolution; Subspace Optimization Method; Perfect Electric Conductor; Metallic Scatterers.

1 Introduction

Detecting metallic objects and retrieving the scatterer shape with microwave imaging techniques is a common task in many practical applications. For instance, the detection of concealed weapons is of paramount importance [1]-[4] in critical environments such as airports and living spaces. In the industrial context, electromagnetic (*EM*) imaging has been used to localize metallic contaminants in food products [5] as well as cracks in metallic pipelines [6]-[8]. As for the medical framework, online sensors have been designed to guide surgeons in the removal of metallic shrapnels [9]. Moreover, subsoil imaging of metallic objects is of great importance for the detection of landmines [10][11] and for the inspection of underground infrastructures [12]-[15].

Generally speaking, metallic objects are, in practice, often modelled as perfect electric conductors (*PECs*) and their *EM* interactions with the probing source have been modeled with reliable techniques in the state-of-the-art literature. Depending on the mathematical modeling, which is a consequence of the representation chosen for the unknown *PEC* objects, the *PEC* imaging methods can be roughly divided in volume-based and surface-based approaches.

In volume-based representations, the investigation domain is discretized in sub-units, namely *pixels*, of unknown dielectric properties to be retrieved by often modeling the field scattered by each *PEC* pixel as a multipole expansion in cylindrical harmonics. For instance, the *Local Shape Function (LSF)* is an example of a volume-based formulation where a boolean variable is associated to each pixel for denoting whether it is *PEC* or empty [16]. Accordingly, the *PEC* inverse scattering problem (*ISP*) is rephrased as a binary optimization one, then solved with Genetic Algorithms (*GAs*) [17][18]. Otherwise, derivative-based optimization algorithms, such as *Conjugate Gradients (CGs)* [16][19][20], are applied when the binary descriptors are relaxed to continuous ones.

In [21], a different volume-based representation is proposed to exploit a fast *Bayesian Compressive Sensing (BCS)* technique for retrieving the 0-th order coefficients of the multipole expansion at each pixel location, which are then post-processed to classify each pixel as *PEC* or empty. Such an approach has been further developed in [22] by considering a multipole expansion of higher order. A higher-order expansion has been also adopted in [23] to solve the *ISP*

involving both *PEC* and dielectric scatterers. Another volume-based representation for mixed targets, which relies on integral scattering equations instead of a multipole expansion, has been presented in [24]-[26]. More specifically, a complex permittivity value has been assigned to each pixel and metallic objects have been modeled as dielectrics with a large, but finite, imaginary part.

Differently from volumetric models, surface-based representations of the *PEC* scatterers only consider the outer contour since it is enough to model the scattering behaviour of objects impenetrable to *EM* waves. Subject to the (also approximate) knowledge of the position and number of disconnected targets, arbitrary *PEC* shapes have been described with either the coefficients of Fourier series [27]-[30] or the control points of spline curves [29]-[34]. In both cases, the surface descriptors have been retrieved by applying the Newton-Kantorovich method [27], the Differential Evolution optimizer [31][33], and the *GAs* [28]-[30][32][34].

Without *a-priori* information on the scattering scenario (i.e., the number and the positions of the objects), the *Level Set (LS)* method has been successfully used in [35] to yield the *PEC* contour. Under the same hypothesis (i.e., without *a-priori* knowledge), another surface-based method, which is based on the discretization of the investigation domain in a grid of segments, has been introduced in [36] and further refined in [37]. Each segment has been then classified as *PEC* or non-*PEC* with an inversion procedure that relies on the *Subspace Optimization Method (SOM)*. Such an approach has been successfully applied to both *TM* and *TE* illuminations [37][39], as well.

Unlike *PEC* inversion methods that require *a-priori* information, which might be inaccurate or even unavailable, the reconstruction approaches that use pixel- or segment-based representations of the investigation domain can effectively model arbitrary connected and non-connected *PEC* geometries, but they need a large number of unknowns to achieve a high-resolution imaging. This causes a heavier ill-posedness of the *ISP* at hand, which implies the use of effective regularization countermeasures, as well as an increase of the computational cost that might result unacceptable (especially) if computationally-intensive optimization methods are adopted for the scattering-data inversion.

To address these issues, a novel strategy, which is based on the Iterative Multi-Scaling Ap-

proach (*IMSA*) as applied to a segment-based representation of the investigation domain of the *ISP*, is proposed hereinafter for the retrieval of *PEC* objects. As a matter of fact, the *IMSA* has been extensively applied to mitigate the non-linearity and to alleviate the non-uniqueness of the *ISP* when dealing with dielectric scatterers [40]-[49]. The underlying idea is that the data inversion is iteratively performed for the reconstruction of only a portion of the whole investigation domain, called *Region of Interest (RoI)*, which is iteratively reduced to implement a synthetic zoom on the scatterers. In this way, the number of unknowns is kept close to the limited amount of information collectable from the measurements [50] for both mitigating the ill-posedness of the *ISP* [40] and reducing the computational burden, but the spatial resolution of the reconstruction is increased only in the *RoIs* where the scatterers have been detected.

Thanks to its flexibility and being a meta-level strategy, the *IMSA* has been integrated with a variety of solution strategies (e.g., the *BCS* [47], the Particle Swarm Optimization [46], and the *SOM* [43][44]) and different formulations (e.g., Lippmann-Schwinger Integral Equations or Contraction Integral Equations [48]). Moreover, it has been used to deal with both two- [49] and three-dimensional [45] inversion problems.

In this paper, the *IMSA* has been combined with the *SOM* to tackle the *PEC* imaging problem since this latter method independently reduces the ill-posedness of the *ISP* [51] by constraining the unknown currents, induced on the investigation domain, to a low-dimensional subspace. Moreover, such an integration has been already successfully exploited for the retrieval of dielectric scatterers [43][44] even though with a pixel-based representation of the investigation domain. Compared to other state-of-the-art techniques, the *IMSA-SOM* tool for the *PEC* reconstruction does not require *a-priori* information on the location or the number of the scatterers and it has limited computational needs thanks to the profitable integration of the *IMSA* with an efficient optimization strategy based on *CG*.

The outline of the paper is as follows. The mathematical formulation of the *ISP* arising in *PEC* imaging is described in Sect. 2, while the proposed *IMSA-SOM* inversion method is detailed in Sect. 3. Section 4 is devoted to the numerical and experimental assessment with some comparisons, as well. Finally, concluding remarks are drawn (Sect. 5).

2 Mathematical Formulation

Let \mathcal{D} be a two-dimensional (2D) square investigation domain of side $\mathcal{L}_{\mathcal{D}}$ laying on the xy -plane within an unbounded free-space background with permittivity and permeability ε_0 and μ_0 , respectively (Fig. 1), where unknown *PEC* scatterers have to be retrieved. Such a scenario is probed by a set of V Transverse Magnetic (*TM*) z -polarized monochromatic (f being the working frequency) plane waves impinging from the angular directions $\{\phi_v; v = 1, \dots, V\}$ and having (known) electric field equal to $\mathbf{E}_{inc}^{(v)}(\mathbf{r}) = E_{inc}^{(v)}(\mathbf{r}) \hat{\mathbf{z}}$ [$\mathbf{r} = (x, y)$] ($v = 1, \dots, V$).⁽¹⁾ For each v -th ($v = 1, \dots, V$) incidence, the electric field⁽²⁾ $\mathbf{E}_{tot}^{(v)}(\mathbf{r}) = E_{tot}^{(v)}(\mathbf{r}) \hat{\mathbf{z}}$ is measured at M positions, $\{\mathbf{r}_m^{(v)}; m = 1, \dots, M\}$, of the observation domain \mathcal{D}_{obs} external to \mathcal{D} .

In order to numerically manage the problem at hand, the investigation domain is partitioned into N square pixels identified by Q line edges (Fig. 1). A binary variable P_q is assigned to each q -th ($q = 1, \dots, Q$) segment to denote the membership to the *PEC* when $P_q = 1$, while $P_q = 0$ stands for the background, so that the dielectric distribution in \mathcal{D} is univocally identified by the algebraic binary vector \overline{P} ($\overline{P} \triangleq \{P_q; q = 1, \dots, Q\}$). From an *EM* viewpoint, each q -th ($q = 1, \dots, Q$) edge is modeled in terms of an associated piece-wise constant equivalent current, $\mathbf{J}^{(v)}(\mathbf{r}_q) = J_z^{(v)}(\mathbf{r}_q) \hat{\mathbf{z}}$, centered at the barycenter of the q -th segment, \mathbf{r}_q , subject to the condition that for each v -th ($v = 1, \dots, V$) view

$$\left(\overline{I} - \overline{\overline{P}}\right) \overline{J}^{(v)} = \overline{0}, \quad (1)$$

which forces the equivalent current to be zero on non-*PEC* segments. In (1), \overline{I} is the identity matrix, $\overline{\overline{P}}$ is the diagonal matrix whose q -th ($q = 1, \dots, Q$) diagonal element is equal to $\overline{P} \Big|_{qq} = P_q$, $\overline{J}^{(v)}$ is the Q -size complex-valued algebraic vector whose q -th ($q = 1, \dots, Q$) entry is equal to $\overline{J}^{(v)} \Big|_q = J_z^{(v)}(\mathbf{r}_q)$, and $\overline{0}$ is the Q -size null vector.

Moreover, the v -th ($v = 1, \dots, V$) scattered field, which is defined as $\mathbf{E}_{sca}^{(v)}(\mathbf{r}) \triangleq \mathbf{E}_{tot}^{(v)}(\mathbf{r}) - \mathbf{E}_{inc}^{(v)}(\mathbf{r})$, is related to the corresponding v -th equivalent current, $\mathbf{J}^{(v)}(\mathbf{r})$, through the following relationship

⁽¹⁾Throughout this paper, a bold notation is used to indicate a physical vector (\mathbf{a}), a single bar indicates an algebraic vector or 1D tensor (\overline{a}), and double bars indicate a matrix or 2D tensor ($\overline{\overline{a}}$).

⁽²⁾Hereinafter, the time-dependency factor $e^{-j2\pi ft}$ is assumed and omitted.

$$\overline{E}_{sca}^{(v)} = \overline{\overline{G}}^{(v)} \overline{J}^{(v)} \quad (2)$$

where $\overline{\overline{G}}$ is the Green's matrix, mapping the equivalent current in \mathbf{r}_q ($q = 1, \dots, Q$) ($\mathbf{r}_q \in \mathcal{D}$) to the scattered field at \mathbf{r}_t , whose (t, q) -th entry is equal to [52]

$$\overline{\overline{G}} \Big|_{tq} = \begin{cases} -\frac{k\eta W}{4} H_0^{(1)}(k \|\mathbf{r}_t - \mathbf{r}_q\|) & \text{if } t \neq q \\ -\frac{k\eta W}{4} \left\{ 1 + j \frac{2}{\pi} \left[\ln \left(\frac{\gamma k W}{4} \right) - 1 \right] \right\} & \text{if } t = q \end{cases}, \quad (3)$$

k ($k \triangleq \frac{2\pi}{\lambda}$) and η ($\eta \triangleq \sqrt{\frac{\mu_0}{\epsilon_0}}$) being the wavenumber and the background impedance, respectively, while λ is the wavelength at f , W is the length of one edge, $H_0^{(1)}$ is the Hankel function of the first kind and 0-th order, $\gamma \approx 1.781$ is a constant [52], and $\|\cdot\|$ stands for the ℓ_2 -norm.

Depending on the location of the probing point \mathbf{r}_t , (2) can be further customized. When $\mathbf{r}_t \in \mathcal{D}_{obs}$ (i.e., $\mathbf{r}_t = \mathbf{r}_m^{(v)}$), (2) is rewritten as

$$\overline{E}_{sca}^{(v)} = \overline{\overline{G}}_{ext}^{(v)} \overline{J}^{(v)} \quad (4)$$

($v = 1, \dots, V$) where $\overline{\overline{G}}_{ext}^{(v)}$ is now a $M \times Q$ matrix with the (m, q) -th ($m = 1, \dots, M$; $q = 1, \dots, Q$) entry given by $\overline{\overline{G}}_{ext}^{(v)} \Big|_{mq} = \overline{\overline{G}} \Big|_{tq}$ ($t \neq q, m = t$), while $\overline{E}_{sca}^{(v)}$ is the complex algebraic vector of size M of the scattered field samples (i.e., $\overline{E}_{sca}^{(v)} = \{E_{sca}^{(v)}(\mathbf{r}_m^{(v)}); m = 1, \dots, M\}$). Otherwise [i.e., $\mathbf{r}_t \in \mathcal{D} \rightarrow \mathbf{r}_t = \mathbf{r}_p$ ($p = 1, \dots, Q$)], it turns out that

$$\overline{E}_{sca}^{(v)} = \overline{\overline{G}}_{int} \overline{J}^{(v)} \quad (5)$$

where $\overline{\overline{G}}_{int}$ is now a $Q \times Q$ matrix with the (p, q) -th ($p, q = 1, \dots, Q$) entry given by $\overline{\overline{G}}_{int} \Big|_{pq} = \overline{\overline{G}} \Big|_{tq}$ ($t = p$), while $\overline{E}_{sca}^{(v)} = \{E_{sca}^{(v)}(\mathbf{r}_q); q = 1, \dots, Q\}$.

Dealing with *PECs*, the boundary condition (i.e., the tangential total field vanishes in correspondence with the *PEC* segments) can be exploited to derive the following

$$\overline{\overline{P}} \left(\overline{E}_{tot}^{(v)} \right) = \overline{0} \quad (6)$$

($v = 1, \dots, V$), where $\overline{E}_{tot}^{(v)} = \{E_{tot}^{(v)}(\mathbf{r}_q); q = 1, \dots, Q\}$. Since $\overline{E}_{tot}^{(v)} = \overline{E}_{inc}^{(v)} + \overline{E}_{sca}^{(v)}$, through (5),

(6) assumes the following form

$$\overline{\overline{P}} \left(\overline{\overline{E}}_{inc}^{(v)} + \overline{\overline{G}}_{int} \overline{\overline{J}}^{(v)} \right) = \overline{0} \quad (7)$$

($v = 1, \dots, V$).

According to such a formulation and the segment-based representation of the *PEC* scatterers, the inverse problem at hand is then rephrased as that of determining $\overline{\overline{P}}$ and $\{\overline{\overline{J}}^{(v)}; v = 1, \dots, V\}$ that fulfil (1), (4), and (7).

3 Inversion Method

The solution of the inverse problem formulated in Sect. 2 is addressed with an approach based on the integration of the *SOM* within the *IMSA* scheme. More specifically, the scattering-data inversion is carried out by means of an iterative strategy that performs S successive “zooming” steps. At each s -th ($s = 1, \dots, S$; s being the step index) step, the *PEC* profile of the *RoI*, which is the portion of the investigation domain \mathcal{D} where the scatterer has been estimated to lie, is retrieved by means of a deterministic algorithm based on the *SOM* as applied to (1), (4), and (7). Such a reconstruction is then exploited to improve the *RoI* estimate by also enhancing the spatial resolution of the retrieval. The process is repeated until a data-matching convergence criterion holds true.

The implementation of such a multi-level process needs: (a) to re-define the problem unknowns, $\{\overline{\overline{P}}; (\overline{\overline{J}}^{(v)}; v = 1, \dots, V)\}$, so that the *SOM*, which is a continuous-variable optimization method, can be fruitfully applied (Sect. “*Unknowns Coding*”); (b) to customize the *SOM* [38] to the problem at hand (Sect. “*SOM Implementation*”); (c) to define a suitable cost function that faithfully links the *ISP* at hand to its mathematical representation so that the solution is the global minimum of the cost function itself (Sect. “*Cost Function Definition*”); (d) to customize the meta-level *IMSA* strategy to both such a formulation (i.e., problem unknowns and cost function) and the integration with the optimization level (i.e., the *SOM*) (Sect. “*IMSA Implementation*”). These items will be detailed or briefly recalled in the following.

Unknowns Coding

Since the unknown vector \bar{P} is binary, it is rewritten as a function of the set of continuous variables, $\{x_q; q = 1, \dots, Q\}$, as follows

$$P_q = \frac{1}{1 + \exp(-bx_q)} \quad (8)$$

($q = 1, \dots, Q$), the coefficient b being defined as in [37]. Consequently, since $x_q > 0$ ($x_q < 0$) implies that $P_q = 1$ ($P_q = 0$), that is, the q -th ($q = 1, \dots, Q$) segment is *PEC* (empty), the same information coded in the Q -size binary vector \bar{P} can be now drawn from the same size continuous vector \bar{x} ($\bar{x} = \{x_q; q = 1, \dots, Q\}$);

SOM Implementation

According to the *SOM* guidelines [51], the v -th ($v = 1, \dots, V$) equivalent current $\bar{J}^{(v)}$ is decomposed in two terms

$$\bar{J}^{(v)} = \bar{J}_D^{(v)} + \bar{J}_A^{(v)}, \quad (9)$$

$\bar{J}_D^{(v)}$ and $\bar{J}_A^{(v)}$ being the deterministic part and the ambiguous one, respectively. The former, $\bar{J}_D^{(v)}$ ($v = 1, \dots, V$), is computed from (4) by applying the singular value decomposition (*SVD*) to the external Green matrix

$$\overline{\overline{G}}_{ext}^{(v)} = \overline{\overline{U}}^{(v)} \overline{\overline{\sigma}}^{(v)} \left(\overline{\overline{V}}^{(v)} \right)^H \quad (10)$$

where H stands for conjugate transposition, $\overline{\overline{U}}^{(v)} = \{\overline{\overline{U}}_q^{(v)}; q = 1, \dots, Q\}$ is the $M \times Q$ matrix whose q -th ($q = 1, \dots, Q$) column is the M -size left-singular vector (i.e., $\overline{\overline{U}}_q^{(v)}$), $\overline{\overline{\sigma}}^{(v)}$ is the $Q \times Q$ diagonal matrix of the Q singular values of $\overline{\overline{G}}_{ext}^{(v)}$ (i.e., $\overline{\overline{\sigma}}^{(v)} = \{\sigma_q^{(v)}; q = 1, \dots, Q\}$), and $\overline{\overline{V}}^{(v)} = \{\overline{\overline{V}}_q^{(v)}; q = 1, \dots, Q\}$ is the $Q \times Q$ matrix whose q -th ($q = 1, \dots, Q$) column is the Q -size right-singular vector (i.e., $\overline{\overline{V}}_q^{(v)}$). More specifically, $\bar{J}_D^{(v)}$ ($v = 1, \dots, V$) is given by

$$\bar{J}_D^{(v)} = \sum_{q=1}^{Q_{th}} \frac{\left(\overline{\overline{U}}_q^{(v)} \right)^H \cdot \overline{\overline{E}}_{sca}^{(v)}}{\sigma_q^{(v)}} \overline{\overline{V}}_q^{(v)} \quad (11)$$

where \cdot denotes the scalar product, while Q_{th} is the *SVD* truncation threshold, which is adap-

tively set as follows [43]

$$Q_{th} = \arg \min_{Q'} \left\{ \left| \frac{\sum_{q=1}^{Q'} \sigma_q^{(v)}}{\sum_{q=1}^Q \sigma_q^{(v)}} - \alpha \right| \right\}, \quad (12)$$

α ($0 < \alpha \leq 1$) being a real user-defined calibration parameter (see Sect. 4.2).

The ambiguous part of the current, $\bar{\mathcal{J}}_A^{(v)}$ ($v = 1, \dots, V$), is yielded as the linear combination of the remaining $(Q - Q_{th})$ right-singular vectors

$$\bar{\mathcal{J}}_A^{(v)} = \sum_{q=Q_{th}+1}^Q w_{q-Q_{th}}^{(v)} \bar{\mathcal{V}}_q^{(v)}, \quad (13)$$

where $\bar{w}^{(v)} = \{w_q^{(v)}; q = 1, \dots, (Q - Q_{th})\}$ is the unknown complex algebraic vector of the weights of the v -th ($v = 1, \dots, V$) ambiguous current, while $\bar{\bar{w}}$ is the corresponding $(Q - Q_{th}) \times V$ size matrix ($\bar{\bar{w}} \triangleq \{\bar{w}^{(v)}; v = 1, \dots, V\}$).

Cost Function Definition

The cost function \mathcal{F} is defined to quantify the mismatch between actual and estimated values in both the scattered field and the induced equivalent currents

$$\mathcal{F}(\bar{x}, \bar{\bar{w}}) = \sum_{v=1}^V \left[\mathcal{F}_{Field}^{(v)}(\bar{x}, \bar{w}^{(v)}) + \mathcal{F}_{Curr}^{(v)}(\bar{x}, \bar{w}^{(v)}) \right] \quad (14)$$

where the term $\mathcal{F}_{Field}^{(v)}$ ($v = 1, \dots, V$) gives the vectorial distance between the measured scattered field, $\bar{E}_{sca}^{(v)}$, and the scattered field yielded from the estimated v -th equivalent current $\bar{\mathcal{J}}^{(v)}$

$$\mathcal{F}_{Field}^{(v)}(\bar{x}, \bar{w}^{(v)}) = \frac{\left\| \bar{E}_{sca}^{(v)} - \bar{\mathcal{G}}_{ext}^{(v)} \bar{\mathcal{J}}^{(v)} \right\|^2}{\left\| \bar{E}_{sca}^{(v)} \right\|^2}, \quad (15)$$

while $\mathcal{F}_{Curr}^{(v)}$ is given by

$$\mathcal{F}_{Curr}^{(v)}(\bar{x}, \bar{w}^{(v)}) = \frac{\left\| (\bar{\mathcal{I}} - \bar{\mathcal{P}}) \bar{\mathcal{J}}^{(v)} \right\|^2}{\left\| \bar{\mathcal{J}}_D^{(v)} \right\|^2} + \frac{\left\| \bar{\mathcal{P}} (\bar{E}_{inc}^{(v)} + \bar{\mathcal{G}}_{int} \bar{\mathcal{J}}^{(v)}) \right\|^2}{\left\| \bar{\mathcal{G}}_{int} \bar{\mathcal{J}}_D^{(v)} \right\|^2} \quad (16)$$

being the normalized error in fulfilling the conditions (1) and (7) on the v -th ($v = 1, \dots, V$) in-

duced equivalent current $\bar{J}^{(v)}$, which is equal to $\bar{J}^{(v)} = \sum_{q=1}^{Q_{th}} \frac{(\bar{U}_q^{(v)})^H \cdot \bar{E}_{sca}^{(v)}}{\sigma_q^{(v)}} \bar{V}_q^{(v)} + \sum_{q=Q_{th}+1}^Q w_{q-Q_{th}}^{(v)} \bar{V}_q^{(v)}$ according to (11) and (13).

IMSA Implementation

The algorithmic customization of the *IMSA* meta-level to integrate the *SOM*-based optimization for the retrieval of *PECs* can be described through the following multi-step iterative (i being the iteration index) process:

- *Initialization* - Set the step index to $s = 1$ and the *RoI* to the whole investigation domain \mathcal{D} ($\mathcal{D}^{(1)} = \mathcal{D}$);
- *IMSA Loop*
 - *Unknowns Setup* ($i = 0$) - If $s = 1$, then set $\bar{w}_i^{(s)} = \bar{x}_i^{(s)} = \bar{0}$. Otherwise (i.e., $s > 1$), map the trial solution from the previous zooming step into the current s -th discretization grid of the *RoI* $\mathcal{D}^{(s)}$ (i.e., $\bar{w}_i^{(s)} = \Phi \left\{ \bar{w}_i^{(s-1)}; \mathcal{D}^{(s)} \right\}$ and $\bar{x}_i^{(s)} = \Phi \left\{ \bar{x}_i^{(s-1)}; \mathcal{D}^{(s)} \right\}$, Φ being the mapping operator from the grid of $\mathcal{D}^{(s-1)}$ to the finer one of $\mathcal{D}^{(s)}$);
 - *Scattering-Data Inversion* - Compute the s -th step trial solution $(\bar{x}^{(s)}, \bar{w}^{(s)})$ within the *RoI* $\mathcal{D}^{(s)}$ by solving the following optimization problem

$$\left(\bar{x}^{(s)}, \bar{w}^{(s)} \right) = \arg \min_{\bar{x}, \bar{w}} \{ \mathcal{F}(\bar{x}, \bar{w}) \} \quad (17)$$

with I iterations of the deterministic two-step *CG* algorithm in [37] (i.e., $\bar{x}^{(s)} = \bar{x}_i^{(s)} \Big|_{i=I}$, $\bar{w}^{(s)} = \bar{w}_i^{(s)} \Big|_{i=I}$) starting from $\bar{x}_i^{(s)} \Big|_{i=0}$ and $\bar{w}_i^{(s)} \Big|_{i=0}$;

- *Step Check* - Stop the *IMSA* loop if the maximum number of zooming steps is reached (i.e., $s = S$) and output the estimated solution by setting $\bar{x}_{opt} = \bar{x}^{(S)}$ and $\bar{w}_{opt} = \bar{w}^{(S)}$;
- *RoI Update* - Compute the s -th estimate of the *PEC* indicator vector $\bar{P}^{(s)}$ through (8) with $x_q \leftarrow x_q^{(s)}$ and apply the “filtering and clustering” operations [40] to determine

the new *RoI*, $\mathcal{D}^{(s+1)}$, by defining its center, $\mathbf{r}_{\mathcal{D}}^{(s+1)}$ [$\mathbf{r}_{\mathcal{D}}^{(s+1)} = (x_{\mathcal{D}}^{(s+1)}, y_{\mathcal{D}}^{(s+1)})$], and side, $\mathcal{L}_{\mathcal{D}}^{(s+1)}$, as follows

$$\xi_{\mathcal{D}}^{(s+1)} = \frac{\sum_{q=1}^Q \xi_q^{(s)} P_q^{(s)}}{\sum_{q=1}^Q P_q^{(s)}} \quad (18)$$

($\xi \in \{x; y\}$) and

$$\mathcal{L}_{\mathcal{D}}^{(s+1)} = 2 \times \frac{\sum_{q=1}^Q \left\| \mathbf{r}_q^{(s)} - \mathbf{r}_{\mathcal{D}}^{(s+1)} \right\| P_q^{(s)}}{\sum_{q=1}^Q P_q^{(s)}}; \quad (19)$$

– *RoI Check* - Terminate the *IMSA* loop if zooming factor $\eta^{(s)}$, which is defined as

$$\eta^{(s)} = \frac{\left| \mathcal{L}_{\mathcal{D}}^{(s+1)} - \mathcal{L}_{\mathcal{D}}^{(s)} \right|}{\mathcal{L}_{\mathcal{D}}^{(s+1)}}, \quad (20)$$

is below a user-defined threshold η_{min} (i.e., $\eta^{(s)} \leq \eta_{min}$) and set the problem solution to the current trial one (i.e., $\bar{x}_{opt} = \bar{x}^{(s)}$ and $\bar{w}_{opt} = \bar{w}^{(s)}$). Otherwise, update the *IMSA* loop index [i.e., $s \leftarrow (s + 1)$] and restart the “*IMSA Loop*”.

4 Numerical and Experimental Validation

This Section is devoted to illustrate the results of the validation of the proposed inversion method and to give some indications on its performance in different scenarios and under various conditions. Towards this end, representative test cases, concerned with both synthetic and experimental scattering data, will be discussed.

To quantitatively assess the effectiveness of the data inversion/reconstructions, suitable error functions, customized to the segment-based representation of *PEC* scatterers, are defined and used. Namely, they are the *total reconstruction error*

$$\Xi_{tot} \triangleq \frac{1}{Q} \sum_{q=1}^Q \left[(1 - P_q^{true}) P_q^{opt} + P_q^{true} (1 - P_q^{opt}) \right] \quad (21)$$

($\Xi_{tot} = 0$ if $\bar{P}^{opt} = \bar{P}^{true}$ and $\Xi_{tot} = 1$ if $\bar{P}^{opt} = \bar{1} - \bar{P}^{true}$), the *internal reconstruction error*

$$\Xi_{int} \triangleq \frac{1}{Q_{int}} \sum_{q=1}^{Q_{int}} P_q^{true} (1 - P_q^{opt}) \quad (22)$$

($\Xi_{int} = 0$ if $P_q^{opt} = 1$ and $\Xi_{int} = 1$ if $P_q^{opt} = 0$, $0 \leq q \leq Q_{int}$), and the *external reconstruction error*

$$\Xi_{ext} \triangleq \frac{1}{Q_{ext}} \sum_{q=1}^{Q_{ext}} (1 - P_q^{true}) P_q^{opt} \quad (23)$$

($\Xi_{int} = 0$ if $P_q^{opt} = 0$ and $\Xi_{int} = 1$ if $P_q^{opt} = 1$, $0 \leq q \leq Q_{ext}$), \overline{P}^{true} and \overline{P}^{opt} being the true/actual and the reconstructed *PEC* indicator vectors, respectively, while $Q_{int} = Q - Q_{ext}$, Q_{ext} being the segments of the investigation domain external to the support of the *PEC* scatterer. Unless stated otherwise, the following reference scenario has been considered throughout the numerical assessment. A measurement setup at a frequency of $f = 300$ [MHz] where a plane wave probes a square investigation domain, \mathcal{D} , of side $\mathcal{L}_{\mathcal{D}} = 3\lambda$ by impinging from $V = 27$ different angular directions $\{\phi_v = 2\pi \frac{(v-1)}{V}; v = 1, \dots, V\}$. The electric field coming from the interaction between the probing source and the scatterers laying in \mathcal{D} has been measured by $M = 27$ ideal probes uniformly-spaced on a circular observation domain, \mathcal{D}_{obs} , external to the investigation domain, with radius $\rho_{obs} = 2.2\lambda$. The $M \times V$ synthetic scattering data have been numerically generated with a Method of Moments (*MoM*) solver by densely discretizing \mathcal{D} with square cells $\lambda/50$ -sided. To emulate real-data, the scattered field samples have been then blurred with an additive white Gaussian noise characterized by a signal-to-noise ratio (*SNR*). According to the guidelines in [50], the inverse problem at hand has been solved by uniformly partitioning \mathcal{D} in $N = 18 \times 18$ sub-domains. Moreover, the maximum number of zooming steps of the *IMSA-SOM* has been set to $S = 6$, while the value of the zooming threshold has been fixed to $\eta_{min} = 0.2$ according to [49].

4.1 Illustrative Example

In this section, a detailed step-by-step description of the *IMSA-SOM* method as applied to an illustrative example is provided. Towards this end, a square *PEC* object of side 0.6λ has been chosen [see the red contour in Fig. 2(a)] and reconstructed by processing noisy scattered data with $SNR = 40$ [dB].

According to the multi-step iterative procedure described in Sect. 3 (“*IMSA Implementation*”), the *RoI* has been first initialized to the whole investigation domain ($\mathcal{D}^{(1)} = \mathcal{D}$). At the first

IMSA step ($s = 1$), a *SOM*-based reconstruction of $\mathcal{D}^{(1)}$ [green pattern - Fig. 2(a)] has been performed. Figure 2(a) shows the reconstructed *PEC* profile with the cyan segments of the *PEC* indicator vector $\overline{P}^{(s)} \Big|_{s=1}$. Starting from such an estimate of the target position and shape, the *RoI* is updated by defining the green patterned region $\mathcal{D}^{(2)}$ in Fig. 2(b). The second ($s = 2$) *IMSA* step has been then carried out by applying the *SOM* inversion to image $\mathcal{D}^{(2)}$. As expected, owing to the improved *RoI* estimate, the reconstructed *PEC* map is significantly closer to the actual one [Fig. 2(b)]. In turn, such an improvement enables a further shrinking of the *RoI*, $\mathcal{D}^{(3)}$, towards the actual support of the *PEC* [Fig. 2(c)]. At the successive *IMSA* step ($s = 3$), the *SOM* inversion is repeated by yielding the *PEC* indicator vector $\overline{P}^{(s)} \Big|_{s=3}$ as mapped in Fig. 2(c). The *IMSA* loop has been then stopped since the zooming factor $(\eta^{(s)}) \Big|_{s=4} = 5.32 \times 10^{-2}$ was below the threshold ($\eta_{min} = 0.2$) as pointed out in Fig. 2(c) where the *RoI* matches very closely the shape of the actual target, and no further reconstruction enhancements were expected further zooming.

For the sake of completeness, the behaviors of both the cost function, \mathcal{F} , and the reconstruction error, Ξ_{tot} , throughout the iterative ($i = 1, \dots, I$) multi-step ($s = 1, \dots, S$) *IMSA-SOM* process are shown in Fig. 3.

4.2 Control-Parameters Calibration

The *IMSA-SOM* inversion method depends on its control parameters (Sect. 3), namely the α threshold, which regulates the adaptive *SVD* truncation process, and the maximum number of iterations of the deterministic two-step *CG* algorithm [37], I , performed at each s -th ($s = 1, \dots, S$) *IMSA* step.

To give the interested readers some insights on the sensitivity of *IMSA-SOM* to these control parameters by also motivating the choice of the control setup used throughout the whole validation, the results of a study on a circular *PEC* object $\lambda/2$ in radius are reported in the following. More in detail, the inversion process has been repeated for each choice of the values of α and I by processing different noisy data so that the inferred indications are independent on the noise level.

The outcomes of such a calibration phase are summarized in Fig. 4 in terms of the total re-

construction error. In particular, Figure 4(a) shows the behavior of Ξ_{tot} versus α when fixing $I = 1000$, while the dependence on I ($\alpha = 0.6$) is analyzed in Fig. 4(b). It turns out [Fig. 4(a)] that the α value impacts significantly on the inversion accuracy, the fluctuations of Ξ_{tot} being quite large since, for instance, $\Xi_{tot} = 0.1$ ($\Xi_{tot} = 0.01$) corresponds to 10(1) % of wrongly reconstructed segments on the total number. To better illustrate such an outcome, let us observe the reconstructions when $\alpha = 0.0$ [Fig. 5(b)] and $\alpha = 1.0$ [Fig. 5(c)]. In the first case, the *SVD* truncation is too selective and only a limited portion of the *PEC* is correctly retrieved [Fig. 5(b)], while there is no truncation when $\alpha = 1.0$ and the inversion generates many artifacts outside the *PEC* domain [Fig. 5(c)].

As for the sensitivity of the *IMSA-SOM* performance on I , Figure 4(b) indicates that, as expected, the higher the I value, the smaller the reconstruction error is, but only until a threshold around ≈ 1000 iterations. Indeed, if the deterministic minimization of \mathcal{F} is stopped too early (e.g., $I = 30$), the optimum of (14) has not yet been reached and the reconstruction is sub-optimal [e.g., Fig. 5(d)]. On the other hand, increasing I beyond a threshold value yields negligible improvements as confirmed by the comparison between the inversion results when setting $I = 1000$ [Fig. 5(a)] or $I = 1500$ [Fig. 5(e)].

The optimal setup for α and I has been then chosen according to the following rule

$$\zeta^{(opt)} = \frac{\int_{SNR} \arg \min_{\zeta} \{ \Xi_{tot} \}_{SNR}^{\zeta} dSNR}{\int_{SNR} dSNR} \quad (24)$$

($\zeta = \{\alpha; I\}$) and the result has been $\alpha_{opt} = 0.6$ and $I_{opt} = 1000$.

A proof of the effectiveness of such a choice is shown in Fig. 5(a) where the *IMSA-SOM* reconstruction when $SNR = 10$ [dB] is reported, the total error being $\Xi_{tot}|_{SNR=10[dB]} = 1.77 \times 10^{-2}$.

4.3 Numerical Assessment

Once calibrated, the performance of the *IMSA-SOM* have been assessed in comparison with a competitive state-of-the-art inversion approach. For a fair comparison, the single-resolution

SOM in [37] has been considered as reference.⁽³⁾

The first test case is concerned with a “T”-shaped *PEC* object is considered whose larger edge is 0.6λ . Such a shape presents corners and cavities making the reconstruction process even harder. Figure 6 shows the behavior of the error indexes versus the *SNR* for both the *IMSA-SOM* and the *SOM*. As it can be noticed, the reconstruction accuracy of the *IMSA*-based method is significantly better than that of the single-resolution *SOM*, the improvement of the total reconstruction error ranging from $\Delta \Xi_{tot} \approx 35 \%$ ($SNR = 40$ [dB]) up to $\Delta \Xi_{tot} \approx 55 \%$ ($SNR = 5$ [dB]) being $\Delta \Xi_{tot} \triangleq \frac{\Xi_{tot}^{SOM} - \Xi_{tot}^{IMSA-SOM}}{\Xi_{tot}^{SOM}}$. Moreover, it turns out that the multi-zooming approach reduces mainly the external error, while the internal one is almost equivalent for both methods. Such an outcome is pictorially pointed out by the map of the retrieved *PEC* profiles in Fig. 7 where the representative examples of inversion when processing data at $SNR = 20$ [dB] [Figs. 7(a)-7(b)], $SNR = 10$ [dB] [Figs. 7(c)-7(d)], and $SNR = 5$ [dB] [Figs. 7(e)-7(f)] are reported. More in detail, the pictures in Figs. 7(a)-7(b) show that both techniques are able to correctly localize the *PEC* object within the investigation domain, but the *IMSA-SOM* better shapes it. The differences between the two inversion approaches become more and more evident increasing the noise level to $SNR = 10$ [dB] [Fig. 7(c) vs. Fig. 7(d)] and up to $SNR = 5$ [dB] [Fig. 7(e) vs. 7(f)] when the *SOM* image reveals some disconnected artifacts in the surrounding of the bottom-left corner of the “T” boundary, as well, so that $\Delta \Xi_{tot} \approx 55 \%$.

The second experiment is aimed at assessing the reliability of the *IMSA-SOM* in reconstructing *PEC* shapes that are not exactly mapped into the gridding of \mathcal{D} . Towards this purpose, a “Diamond” object with diagonal equal to $d = 0.5 \lambda$ and edges tilted with respect to the discretization grid has been considered as benchmark. The results in Fig. 8 indicate that the *IMSA-SOM* reduces the value of the total error of the *SOM* up to $\Delta \Xi_{tot} \approx 61 \%$ ($SNR = 5$ [dB]), the minimum improvement being equal to $\Delta \Xi_{tot} \approx 47 \%$ ($SNR = 40$ [dB]). Moreover, the (expected) worsening of the reconstruction accuracy for higher and higher level of noise is more contained (i.e., $\Delta \delta_{tot}^{IMSA-SOM} \approx 62 \%$ vs. $\Delta \delta_{tot}^{IMSA-SOM} \approx 73 \%$ being $\Delta \delta_{tot} \triangleq \frac{\Xi_{tot}|_{SNR=5[dB]} - \Xi_{tot}|_{SNR=40[dB]}}{\Xi_{tot}|_{SNR=5[dB]}}$).

Such an enhanced robustness to the noise blurring the data is also highlighted in Figs. 9(a)-9(f)

⁽³⁾According to the guidelines in [37], a $\lambda/10$ -sided uniform grid has been chosen to discretize the investigation domain \mathcal{D} for the single-resolution inversion so that ($N^{SOM} = 30 \times 30$).

since the *SOM* profiles are increasingly over-estimated as the *SNR* reduces [Fig. 9(b), Fig. 9(d), and Fig. 9(f)], while there are little differences in both size and shape when applying the *IMSA-SOM*. This latter mainly derives from the ability of the *IMSA* to model more accurately the tilted edges of the diamond contour thanks to the use of a denser discretization in the *RoI*. Still referring to the “Diamond” *PEC*, the dependence of the *IMSA-SOM* inversion on the size of the scatterer has been evaluated next by varying the diagonal, d , between $d = 0.1 \lambda$ and $d = 1.5 \lambda$. Figure 10 gives the values of the total reconstruction error, Ξ_{tot} , versus d for different *SNRs*. It turns out that, whatever the combination of the target size and the noise level, the *IMSA-SOM* performs better than the *SOM*. However, it is worth noticing that, while the error values tend to be quite close for larger dimensions of the *PEC* ($\frac{d}{\lambda} \rightarrow 1.5$) and high *SNRs*, the advantage of using the *IMSA* strategy becomes greater as the size is lowered and the noise level is getting heavier.

To further confirm these conclusions, Figures 11(a)-11(f) show the *PEC* profiles retrieved when processing data with $SNR = 5$ [dB]. When $d = 1.1 \lambda$ [Figs. 11(a)-11(b)], the *SOM* image presents both spurious artifacts outside the actual contour and a wrong empty internal region, which are properly avoided by the *IMSA-SOM*. Moving to the case $d = 0.7 \lambda$, the *IMSA-SOM* confirms to be more accurate in shaping the actual scatterer as well as in estimating its support [Fig. 11(c) vs. Fig. 11(d)]. This is even more evident when $d = 0.3 \lambda$ [Fig. 11(e) vs. Fig. 11(f)].

The successive experiment has been devoted to infer the highest spatial resolution, R (i.e., the minimum distance at which two disconnected objects can be distinguished), achievable by the *IMSA-SOM*. More specifically, two *PEC* circles of radius 0.1λ have been considered and the minimum distance between their boundaries, D , has been varied within the range $0.3 \lambda \leq D \leq 0.7 \lambda$.

Figure 12 shows the total reconstruction error, Ξ_{tot} , as a function of the object distance, D , when $SNR = 20$ [dB]. Unlike the *IMSA-SOM*, where the Ξ_{tot} is almost flat in all the range of variation of D and equal to $\Xi_{tot}^{IMSA-SOM} \approx 0.01$, the plot of the *SOM* error shows a hill-like behavior with $\Delta \Xi_{tot} \geq 55 \%$ when $\frac{D}{\lambda} \leq 0.57$. Figures 13(a)-13(f) illustrate these deductions by showing the profiles reconstructed in correspondence with three representative values of D , namely

$D = 0.5 \lambda$ [Figs. 13(a)-13(b)], $D = 0.35 \lambda$ [Figs. 13(c)-13(d)], and $D = 0.3 \lambda$ [Figs. 13(e)-13(f)]. When the inter-objects distance is $D = 0.5 \lambda$, both single and multi-resolution *SOM* techniques distinguish two separated scatterers [Figs. 13(a)-13(b)], even though the “bare” *SOM* overestimates the size of the circles and it also retrieves spurious artifacts in the proximity of the actual *PECs* [Fig. 13(b)]. Decreasing the distance below $D \approx 0.5 \lambda$ [e.g., $D = 0.35 \lambda$ - Fig. 13(d)], the single-resolution is no more able to recognize two objects as correctly done by the *IMSA*-based inversion [Fig. 13(c) vs. Fig. 13(d)]. If D is further shortened [e.g., $D = 0.30 \lambda$ - Figs. 13(e)-13(f)], neither of the two methods can resolve the two disconnected supports. However, while the *IMSA-SOM* map in Fig. 13(e) shows some “ghost” shadows in between the *PEC* circles, the *SOM* also detects wrong artifacts far from the actual scatterers [Fig. 13(f)].

Similar results have been obtained in other test cases during an exhaustive numerical assessment, thus we are quite confident to state that the spatial resolution of the *IMSA-SOM* is $R^{IMSA-SOM} = 0.35 \lambda$, that is a 30 % improvement over the single-resolution *SOM* being $R^{SOM} = 0.5 \lambda$.

4.4 Experimental Assessment

After the numerical validation with synthetic scattering data, this section is devoted to the assessment of the *IMSA-SOM* inversion strategy against experimental data measured in a real environment. Towards this end, the “rectTM_cent” and “rectTM_dece” datasets, provided by the Institut Fresnel, have been considered [53]. These two datasets have been generated by measuring the *EM* interactions between a metallic cylinder of section $1.27 \text{ [cm]} \times 2.45 \text{ [cm]}$ and the *EM* field radiated by a horn antenna located 72 [cm] away and working at $f = 8 \text{ [GHz]}$. More in detail, the scatterer under test has been illuminated from $V = 36$ different angular directions, while the scattered electric field has been collected by $M = 49$ measurement probes uniformly located on a circular observation domain \mathcal{D}_{obs} of radius $\rho_{obs} = 76 \text{ [cm]}$. The two datasets differ for the position of the object with respect to the center of the measurements systems (i.e., $(x_0, y_0) = (-0.5, -0.75) \text{ [cm]}$ - Dataset “rectTM_cent”; $(x_0, y_0) = (0, 4) \text{ [cm]}$ - Dataset “rectTM_dece”).

The inversions of the “rectTM_cent” dataset are shown in Figs. 14(a)-14(b). One can observe that both methods correctly localize the unknown object, but the *SOM* gets worse since (once again) it overestimates the size of the cylinder as confirmed by the values of the total reconstruction error, Ξ_{tot} , in Tab. I (i.e., $\Delta\Xi_{tot} \approx 55\%$).

Concerning the computational issues, it turns out that the *IMSA-SOM* allows a computational saving⁽⁴⁾ with respect to the bare *SOM* of about $\Delta t \approx 77\%$ ($\Delta t \triangleq \frac{\mathcal{T}^{SOM} - \mathcal{T}^{IMSA-SOM}}{\mathcal{T}^{SOM}}$). Indeed, even though the *IMSA-SOM* repeats up to $S = 6$ times the inversion process, while the *SOM* does it only once, the dimension of the inversion problem at hand is much smaller (i.e., $N^{IMSA-SOM} \ll N^{SOM}$) despite the higher spatial resolution yielded at the convergence.

Similar outcomes can be drawn for the “rectTM_dece” dataset, the *IMSA-SOM* improvements in both reconstruction accuracy and computational costs being $\Delta\Xi_{tot} \approx 50\%$ and $\Delta t \approx 72\%$ (Tab. I). For completeness, the *PEC* profiles retrieved by the multi-resolution/steps and the single-step *SOM* implementations are shown in Fig. 15.

5 Conclusions

A novel inversion strategy, named *IMSA-SOM*, has been developed to address the *ISP* for *2D* *PECs*. The proposed strategy combines the *IMSA* and the *SOM* and it has proved to be reliable and highly effective in a wide range of scenarios and under different conditions. Indeed, the developed inversion approach has been tested against both numerical and experimental scattering data by considering complex shapes and closely-located scatterers, as well.

Compared to the state-of-the-art literature on the subject, to the best of the authors’ knowledge, the main outcome of this paper and of the related research work is that the developed innovative method for the *PEC* reconstruction is a reliable, flexible, and computationally efficient inversion tool, robust to the noise on the scattering data, as well, that effectively mitigates the non-linearity and the ill-posedness of the imaging problem at hand.

Future works, beyond the scope of the current manuscript, will be aimed at extending the formulation to three-dimensional (*3D*) geometries as well as at customizing the proposed implementation to buried objects scenarios of great applicative interest.

⁽⁴⁾On a standard laptop computer with i5-8265U processor and 8 [GB] RAM.

Acknowledgements

This work has been partially supported by the Italian Ministry of Education, University, and Research within the PRIN 2017 Program, for the Project “Cloaking Metasurfaces for a New Generation of Intelligent Antenna Systems (MANTLES)” (Grant No. 2017BHFZKH - CUP: E64I19000560001) and the Project "CYBER-PHYSICAL ELECTROMAGNETIC VISION: Context-Aware Electromagnetic Sensing and Smart Reaction (EMvisioning)" (Grant no. 2017HZJXSZ - CUP: E64I19002530001), within the Program "Progetti di Ricerca Industriale e Sviluppo Sperimentale nelle 12 aree di specializzazione individuate dal PNR 2015-2020", Specialization Area "Smart Secure & Inclusive Communities" for the Project "Mitigazione dei rischi naturali per la sicurezza e la mobilita' nelle aree montane del Mezzogiorno (MITIGO)" (Grant no. ARS01_00964), and within the Program "Smart cities and communities and Social Innovation" for the Project "Piattaforma Intelligente per il Turismo (SMARTOUR)" (Grant no. SCN_00166 - CUP: E44G14000040008). Moreover, it benefited from the networking activities carried out within the Project “SPEED” (Grant No. 61721001) funded by National Science Foundation of China under the Chang-Jiang Visiting Professorship Program. A. Massa wishes to thank E. Vico for her never-ending inspiration, support, guidance, and help.

References

- [1] T. Liu, Y. Zhao, Y. Wei, Y. Zhao, and S. Wei, “Concealed object detection for activate millimeter wave image,” *IEEE Trans. Ind. Electron.*, vol. 66, no. 12, pp. 9909-9917, Dec. 2019.
- [2] Z. Briqech, S. Gupta, A.-A. Beltay, A. Elboushi, A.-R. Sebak, and T. A. Denidni, “57-64 GHz imaging/detection sensor–part II: experiments on concealed weapons and threatening materials detection,” *IEEE Sensors J.*, vol. 20, no. 18, pp. 10833-10840, Sep. 2020.
- [3] A. Zhuravlev, V. Razevig, M. Chizh, G. Dong, and B. Hu, “A new method for obtaining radar images of concealed objects in microwave personnel screening systems,” *IEEE Trans. Microw. Theory Techn.*, vol. 69, no. 1, pp. 357-364, Jan. 2021.

- [4] C. Wang, J. Shi, Z. Zhou, L. Li, Y. Zhou, and X. Yang, "Concealed object detection for millimeter-wave images with normalized accumulation map," *IEEE Sensors J.*, vol. 21, no. 5, pp. 6468-6475, Mar. 2021.
- [5] G. Ok, H. J. Kim, H. S. Chun, and S.-W. Choi, "Foreign-body detection in dry food using continuous sub-terahertz wave imaging," *Food Control*, vol. 42, pp. 284-289, Aug. 2014.
- [6] R. K. Amineh, N. K. Nikolova, J. P. Reilly, and J. R. Hare, "Characterization of surface-breaking cracks using one tangential component of magnetic leakage field measurements," *IEEE Trans. Magn.*, vol. 44, no. 4, pp. 516-524, Apr. 2008.
- [7] M. Norouzi, N. Masoumi, and H. Jahed, "Nondestructive phase variation-based chipless sensing methodology for metal crack monitoring," *IEEE Trans. Instrum. Meas.*, vol. 70, pp. 1-11, Mar. 2021.
- [8] Z. Chen, X. Q. Lin, Y. H. Yan, F. Xiao, M. T. Khan, and S. Zhang, "Noncontact group-delay-based sensor for metal deformation and crack detection," *IEEE Trans. Ind. Electron.*, vol. 68, no. 8, pp. 7613-7619, Aug. 2021.
- [9] M. Sakthivel, B. George, and M. Sivaprakasam, "A new inductive proximity sensor based guiding tool to locate metal shrapnel during surgery," *IEEE Trans. Instrum. Meas.*, vol. 63, no. 12, pp. 2940-2949, Dec. 2014.
- [10] J. R. Bourgeois and G. S. Smith, "A complete electromagnetic simulation of the separated-aperture sensor for detecting buried land mines," *IEEE Trans. Antennas Propag.*, vol. 46, no. 10, pp. 1419-1426, Oct. 1998.
- [11] R. Bansal, "Of mice and men [Microwave surfing]," *IEEE Microw. Mag.*, vol. 16, no. 11, pp. 18-20, Dec. 2015.
- [12] M. R. Shaw, S. G. Millard, T. C. K. Molyneaux, M. J. Taylor, and J. H. Bungey, "Location of steel reinforcement in concrete using ground penetrating radar and neural networks," *NDT E Int.*, vol. 38, no. 3, pp. 203-212, Apr. 2005.

- [13] Y. Chen, Y. Chen, C. Chiu, and C. Chang, "Image reconstruction of a buried perfectly conducting cylinder illuminated by transverse electric waves," *Int. J. Imag. Syst. Technol.*, vol. 15, no. 6, pp. 261-265, Apr. 2006.
- [14] A. Zitouni, L. Beheim, R. Huez, and F. Belloir, "Smart electromagnetic sensor for buried conductive targets identification," *IEEE Sensors J.*, vol. 6, no. 6, pp. 1580-1591, Dec. 2006.
- [15] F. Sheikhi, D. Spinello, and W. Gueaieb, "Renyi entropy filter for anomaly detection with eddy current remote field sensors," *IEEE Sensors J.*, vol. 15, no. 11, pp. 6399-6408, Nov. 2015.
- [16] W. C. Chew and G. P. Otto, "Microwave imaging of multiple conducting cylinders using local shape functions," *IEEE Microwave Guided Wave Lett.*, Vol. 2, pp. 284-286, Jul. 1992.
- [17] Y. Zhou and H. Ling, "Electromagnetic inversion of ipswich objects with the use of the genetic algorithm," *Microw. Opt. Technol. Lett.*, vol. 33, no. 6, pp. 457-459, Jun. 2002.
- [18] T. Takenaka, Z. Q. Meng, T. Tanaka, and W. C. Chew, "Local shape function combined with genetic algorithm applied to inverse scattering for strips," *Microw. Opt. Technol. Lett.*, vol. 16, no. 6, pp. 337-341, Dec. 1997.
- [19] W. H. Weedon and W. C. Chew, "Time-domain inverse scattering using the local shape function (LSF) method," *Inv. Prob.*, vol. 9, pp. 551-564, Oct. 1993.
- [20] G. P. Otto and W. C. Chew, "Microwave inverse scattering—Local shape function imaging for improved resolution of strong scatterers," *IEEE Trans. Microwave Theory Tech.*, vol. 42, no. 1, pp. 137-141, Jan. 1994.
- [21] L. Poli, G. Oliveri, and A. Massa, "Imaging sparse metallic cylinders through a local shape function Bayesian compressive sensing approach," *J. Opt. Soc. Amer. A.*, vol. 30, no. 6, pp. 1261, Jun. 2013.

- [22] M. N. Stevanovic, L. Crocco, A. R. Djordjevic, and A. Nehorai, "Higher order sparse microwave imaging of PEC scatterers," *IEEE Trans. Antennas Propag.*, vol. 64, no. 3, pp. 988-997, Mar. 2016.
- [23] X. Z. Ye, X. Chen, Y. Zhong, and R. C. Song, "Simultaneous reconstruction of dielectric and perfectly conducting scatterers via T-matrix method," *IEEE Trans. Antennas Propag.*, vol. 61, no. 7, pp. 3774-3781, Jul. 2013.
- [24] C. Yu, L. P. Song, and Q. H. Liu, "Inversion of multi-frequency experimental data for imaging complex objects by a DTA-CSI method," *Inverse Probl.*, vol. 21, no. 6, pp. S165-S178, Dec. 2005.
- [25] R. Azaro, M. Donelli, D. Franceschini, and A. Massa, "Multiscaling reconstruction of metallic targets from TE and TM experimental data," *Microw. Opt. Technol. Lett.*, vol. 48, no. 2, pp. 322-324, Feb. 2006.
- [26] S. Sun, B. J. Kooij, and A. G. Yarovoy, "A linear model for microwave imaging of highly conductive scatterers," *IEEE Trans. Microw. Theory Techn.*, vol. 66, no. 3, pp. 1149-1164, Mar. 2018.
- [27] A. Roger, "Newton-Kantorovitch algorithm applied to an electromagnetic inverse problem," *IEEE Trans. Antennas Propag.*, vol. 29, no. 2, pp. 232-238, Mar. 1981.
- [28] C. C. Chiu and P. T. Liu, "Image reconstruction of a perfectly conducting cylinder by the genetic algorithm," *IEE Proc. Microw. Antennas Propag.*, vol. 143, no. 3, pp. 249, Jun. 1996.
- [29] W. Chien, C. H. Huang, and C. C. Chiu, "Cubic-spline expansion for a two-dimensional periodic conductor in free space," *Int. J. Appl. Electromagn. Mechanics*, vol. 24, no. 1-2, pp. 105-114, Dec. 2006.
- [30] W. Chien, C. C. Chiu, and C. L. Li, "Cubic-spline expansion for a conducting cylinder buried in a slab medium," *Electromagnetics*, vol. 26, no. 5, pp. 329-343, 2006.

- [31] A. Qing, "Electromagnetic inverse scattering of multiple two-dimensional perfectly conducting objects by the differential evolution strategy," *IEEE Trans. Antennas Propag.*, vol. 51, no. 6, pp. 1251-1262, Jun. 2003.
- [32] Y. Zhou, J. Li, and H. Ling, "Shape inversion of metallic cavities using hybrid genetic algorithm combined with tabu list," *Electron. Lett.*, vol. 39, no. 3, pp. 280, 2003.
- [33] A. Qing, "Electromagnetic inverse scattering of multiple perfectly conducting cylinders by differential evolution strategy with individuals in groups (GDES)," *IEEE Trans. Antennas Propag.*, vol. 52, no. 5, pp. 1223-1229, May 2004.
- [34] W. Chien and C.-C. Chiu, "Using NU-SSGA to reduce the searching time in inverse problem of a buried metallic object," *IEEE Trans. Antennas Propag.*, vol. 53, no. 10, pp. 3128-3134, Oct. 2005.
- [35] A. Litman, D. Lesselier, and F. Santosa, "Reconstruction of a two-dimensional binary obstacle by controlled evolution of a level-set," *Inverse Probl.*, vol. 14, no. 3, pp. 685-706, Jun. 1998.
- [36] X. Ye, X. Chen, Y. Zhong, and K. Agarwal, "Subspace-based optimization method for reconstructing perfectly electric conductors," *Prog. Electromag. Res.*, vol. 100, pp. 119-128, 2010.
- [37] X. Z. Ye, Y. Zhong, and X. Chen, "Reconstructing perfectly electric conductors by the subspace-based optimization method with continuous variables," *Inverse Probl.*, vol. 27, no. 5, pp. 055011, May 2011.
- [38] X. Chen, *Computational methods for electromagnetic inverse scattering*. Singapore: Wiley, 2018.
- [39] J. Shen, Y. Zhong, X. Chen, and L. Ran, "Inverse scattering problems of reconstructing perfectly electric conductors with TE illumination," *IEEE Trans. Antennas Propag.*, vol. 61, no. 9, pp. 4713-4721, Sep. 2013.

- [40] S. Caorsi, M. Donelli, D. Franceschini, and A. Massa, "A new methodology based on an iterative multiscaling for microwave imaging," *IEEE Trans. Microw. Theory Techn.*, vol. 51, no. 4, pp. 1162-1173, Apr. 2003.
- [41] P. Rocca, M. Donelli, G. L. Gragnani, and A. Massa, "Iterative multi-resolution retrieval of non-measurable equivalent currents for the imaging of dielectric objects," *Inverse Probl.*, vol. 25, no. 5, pp. 055004, May 2009.
- [42] M. Donelli, G. Franceschini, A. Martini, and A. Massa, "An integrated multiscaling strategy based on a particle swarm algorithm for inverse scattering problems," *IEEE Trans. Geosci. Remote Sens.*, vol. 44, no. 2, pp. 298-312, Feb. 2006.
- [43] G. Oliveri, Y. Zhong, X. Chen, and A. Massa, "Multiresolution subspace-based optimization method for inverse scattering problems," *J. Opt. Soc. Amer. A*, vol. 28, no. 10, pp. 2057-2069, Oct. 2011.
- [44] X. Ye, L. Poli, G. Oliveri, Y. Zhong, K. Agarwal, A. Massa, and X. Chen, "Multi-resolution subspace-based optimization method for solving three-dimensional inverse scattering problems," *J. Opt. Soc. Amer. A*, vol. 32, no. 11, pp. 2218-2226, Nov. 2015.
- [45] M. Salucci, G. Oliveri, N. Anselmi, F. Viani, A. Fedeli, M. Pastorino, and A. Randazzo, "Three-dimensional electromagnetic imaging of dielectric targets by means of the multiscaling inexact-newton method," *J. Opt. Soc. Amer. A.*, vol. 34, no. 7, pp. 1119, Jul. 2017.
- [46] M. Salucci, L. Poli, N. Anselmi and A. Massa, "Multifrequency particle swarm optimization for enhanced multiresolution GPR microwave imaging," *IEEE Trans. Geosci. Remote Sens.*, vol. 55, no. 3, pp. 1305-1317, Mar. 2017.
- [47] N. Anselmi, L. Poli, G. Oliveri, and A. Massa, "Iterative multiresolution Bayesian CS for microwave imaging," *IEEE Trans. Antennas Propag.*, vol. 66, no. 7, pp. 3665-3677, Jul. 2018.
- [48] Y. Zhong, M. Salucci, K. Xu, A. Polo, and A. Massa, "A multiresolution contraction integral equation method for solving highly nonlinear inverse scattering problems," *IEEE Trans. Microw. Theory Techn.*, vol. 68, no. 4, pp. 1234-1247, Apr. 2020.

- [49] M. Salucci, C. Estatico, A. Fedeli, G. Oliveri, M. Pastorino, S. Povoli, A. Randazzo, and P. Rocca, "2-D TM GPR imaging through a multiscaling multifrequency approach in L^p spaces," *IEEE Trans. Geosci. Remote Sens.*, vol. 59, no. 12, pp. 10011-10021, Dec. 2021.
- [50] O. M. Bucci and T. Isernia, "Electromagnetic inverse scattering: retrievable information and measurement strategies," *Radio Sci.*, vol. 32, no. 6, pp. 2123-2137, 1997.
- [51] X. Chen, "Application of signal-subspace and optimization methods in reconstructing extended scatterers," *J. Opt. Soc. Amer. A*, vol. 26, no. 4, pp. 1022-1026, Apr. 2009.
- [52] A. F. Peterson, S. L. Ray, and R. Mittra, *Computational methods for electromagnetics*. New York, NY: IEEE Press, 1998.
- [53] K. Belkebir and M. Saillard, "Special section: testing inversion algorithms against experimental data," *Inverse Probl.*, vol. 17, no. 6, pp. 1565-1571, Dec. 2001.

FIGURE CAPTIONS

- **Figure 1.** *Problem Scenario* - 2D *TM* imaging Setup.
- **Figure 2.** *Illustrative Example* (“Square” *PEC* object, $M = V = 27$) - *RoI* and *PEC* map retrieved at different zooming steps of the *IMSA-SOM* algorithm: (a) $s = 1$, (b) $s = 2$, and (c) $s = 3$.
- **Figure 3.** *Illustrative Example* (“Square” *PEC* object, $M = V = 27$; *IMSA-SOM*) - Plots of the cost function, \mathcal{F} , and the total reconstruction error, Ξ_{tot} , versus the iteration index ($i = 1, \dots, I$; $s = 1, \dots, S$).
- **Figure 4.** *Control-Parameters Calibration* (“Circle” *PEC* object, $M = V = 27$) - Plots of the total reconstruction error, Ξ_{tot} , as a function of (a) α ($I = 1000$) and (b) I ($\alpha = 0.6$).
- **Figure 5.** *Control-Parameters Calibration* (“Circle” *PEC* object, $M = V = 27$, $SNR = 10$ [dB]; *IMSA-SOM*) - Maps of the *PEC* profile reconstructed when setting (a) $\alpha = 0.6$ and $I = 1000$, (b) $\alpha = 0.0$ and $I = 1000$, (c) $\alpha = 1.0$ and $I = 1000$, (d) $\alpha = 0.6$ and $I = 30$, and (e) $\alpha = 0.6$ and $I = 1500$.
- **Figure 6.** *Numerical Assessment* (“T” *PEC* object, $M = V = 27$) - Plots of the reconstruction error indexes versus the SNR value.
- **Figure 7.** *Numerical Assessment* (“T” *PEC* object, $M = V = 27$) - Maps of the *PEC* profile retrieved by (a)(c)(e) the *IMSA-SOM* and (b)(d)(f) the *SOM* when processing noisy scattering data with (a)(b) $SNR = 20$ [dB], (c)(d) $SNR = 10$ [dB], and (e)(f) $SNR = 5$ [dB].
- **Figure 8.** *Numerical Assessment* (“Diamond” *PEC* object, $d = 0.5\lambda$, $M = V = 27$) - Plots of the reconstruction error indexes versus the SNR value.
- **Figure 9.** *Numerical Assessment* (“Diamond” *PEC* object, $d = 0.5\lambda$, $M = V = 27$) - Maps of the *PEC* profile retrieved by (a)(c)(e) the *IMSA-SOM* and (b)(d)(f) the *SOM* when processing noisy scattering data with (a)(b) $SNR = 20$ [dB], (c)(d) $SNR = 10$ [dB], and (e)(f) $SNR = 5$ [dB].

- **Figure 10.** *Numerical Assessment* (“Diamond” *PEC* object, $M = V = 27$) - Plots of the reconstruction error indexes as a function of the diagonal of the scatterer, d .
- **Figure 11.** *Numerical Assessment* (“Diamond” *PEC* object, $M = V = 27$, $SNR = 5$ [dB]) - Maps of the *PEC* profile retrieved by (a)(c)(e) the *IMSA-SOM* and (b)(d)(f) the *SOM* when processing the data scattered by the actual object with diagonal (a)(b) $d = 1.1 \lambda$, (c)(d) $d = 0.7 \lambda$, and (e)(f) $d = 0.3 \lambda$.
- **Figure 12.** *Numerical Assessment* (“Two Circles” *PEC* objects, $M = V = 27$, $SNR = 20$ [dB]) - Plots of the total reconstruction error, Ξ_{tot} , as a function of the inter-scatterers distance, D .
- **Figure 13.** *Numerical Assessment* (“Two Circles” *PEC* objects, $M = V = 27$, $SNR = 20$ [dB]) - Maps of the *PEC* profile retrieved by (a)(c)(e) the *IMSA-SOM* and (b)(d)(f) the *SOM* when processing the data scattered by the actual *PEC* objects spaced by (a)(b) $D = 0.50 \lambda$, (c)(d) $D = 0.35 \lambda$, and (e)(f) $D = 0.30 \lambda$.
- **Figure 14.** *Experimental Assessment* (Dataset “rectTM_cent”, $V = 36$, $M = 49$) - Maps of the *PEC* profile retrieved by (a) the *IMSA-SOM* and (b) the *SOM*.
- **Figure 15.** *Experimental Assessment* (Dataset “rectTM_dece”, $V = 36$, $M = 49$) - Maps of the *PEC* profile retrieved by (a) the *IMSA-SOM* and (b) the *SOM*.

TABLE CAPTIONS

- **Table I.** *Experimental Assessment* ($V = 36$, $M = 49$) - Reconstruction error indexes and CPU time.

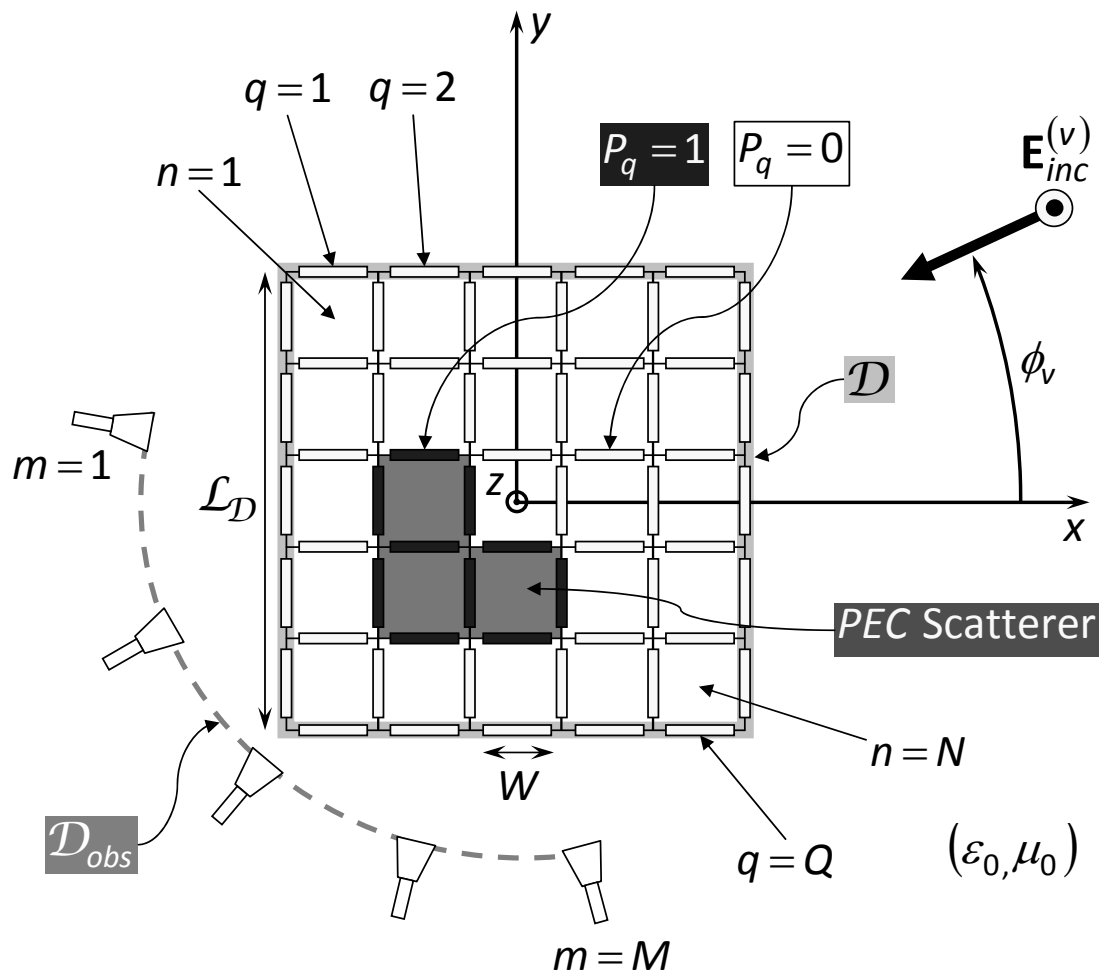


Fig. 1 - Ye et al., "Multi-Resolution Subspace-Based ..."

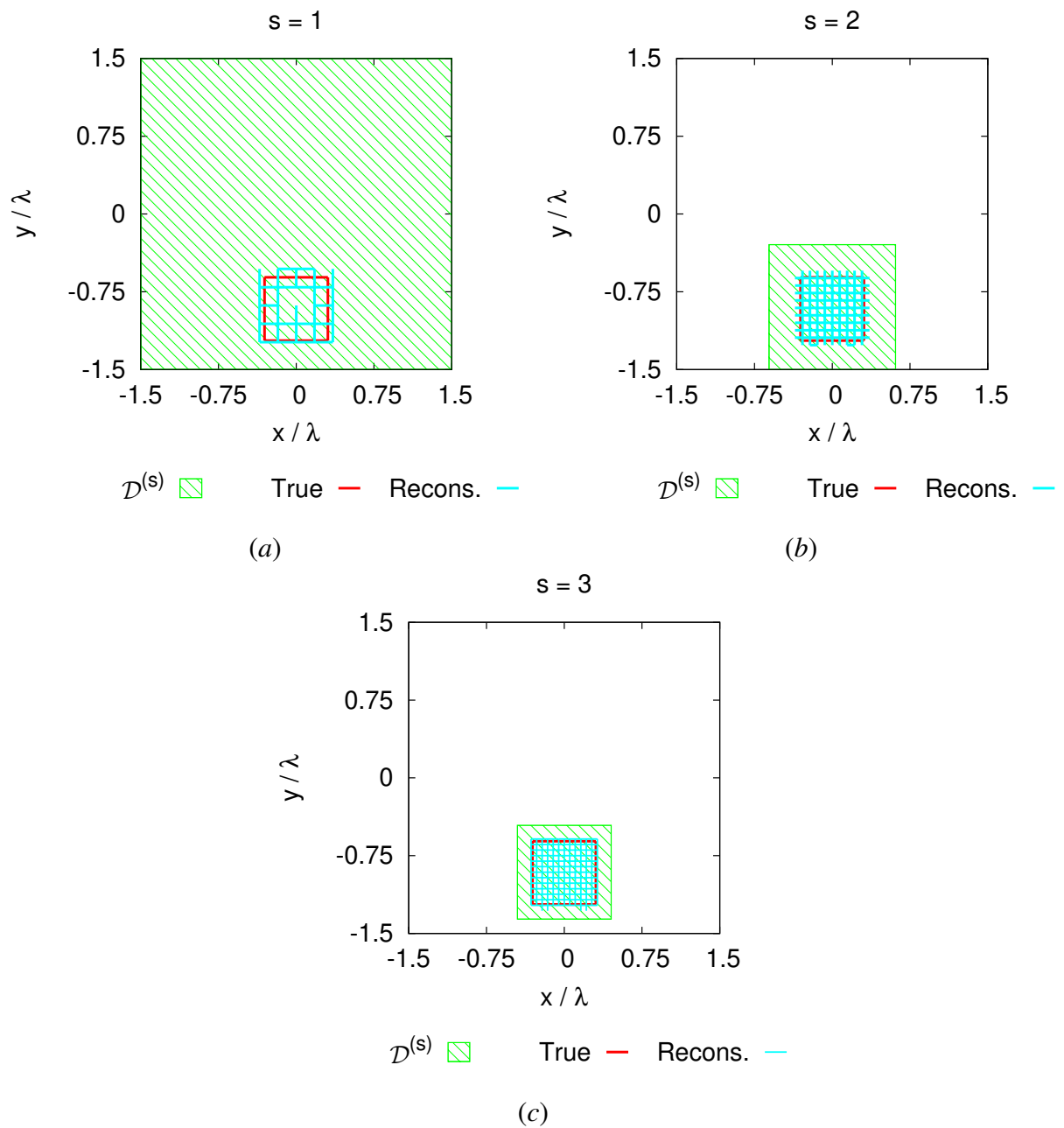


Fig. 2 - Ye et al., “Multi-Resolution Subspace-Based ...”

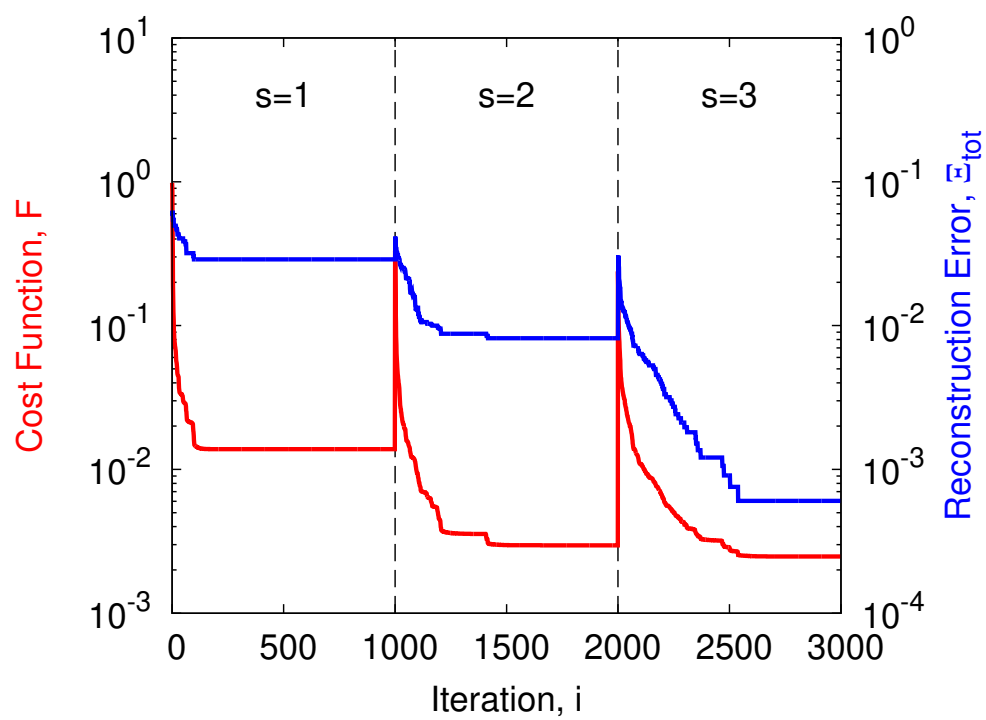
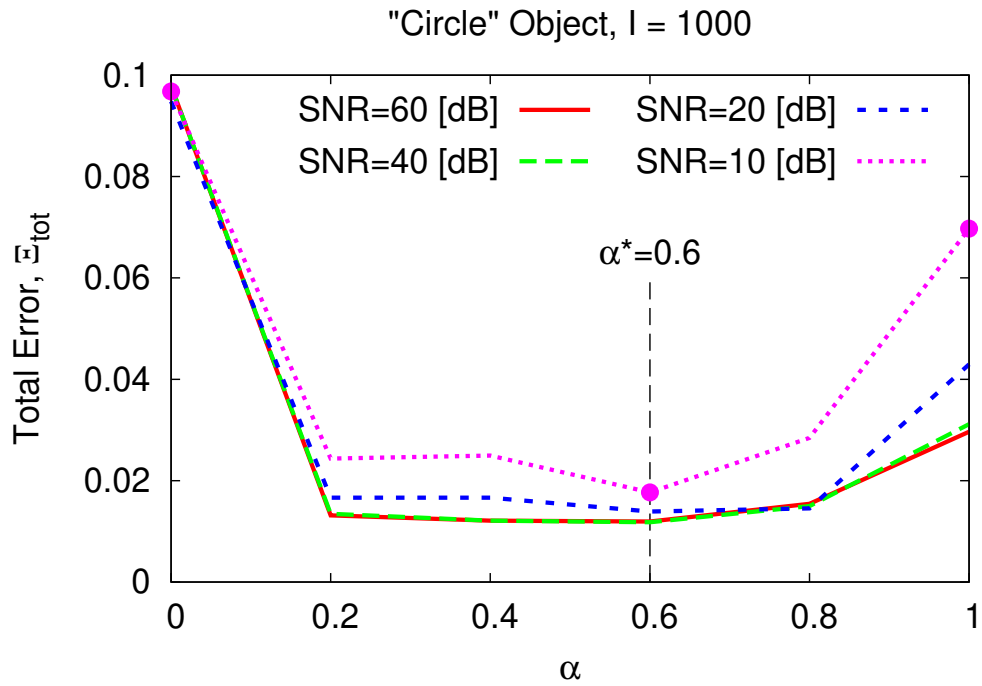
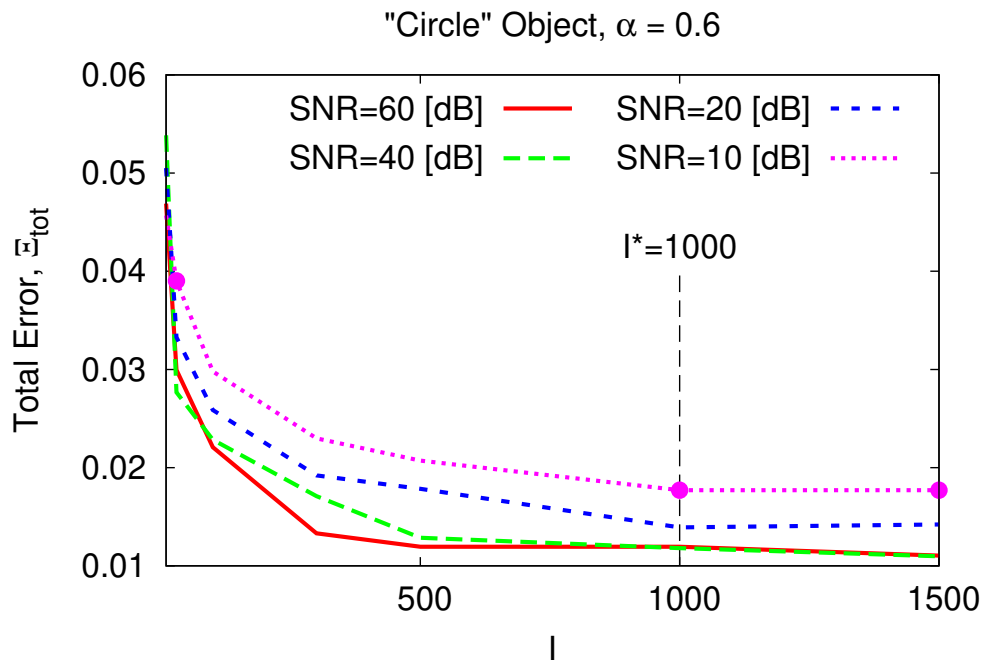


Fig. 3 - Ye et al., “Multi-Resolution Subspace-Based ...”



(a)



(b)

Fig. 4 - Ye et al., "Multi-Resolution Subspace-Based ..."

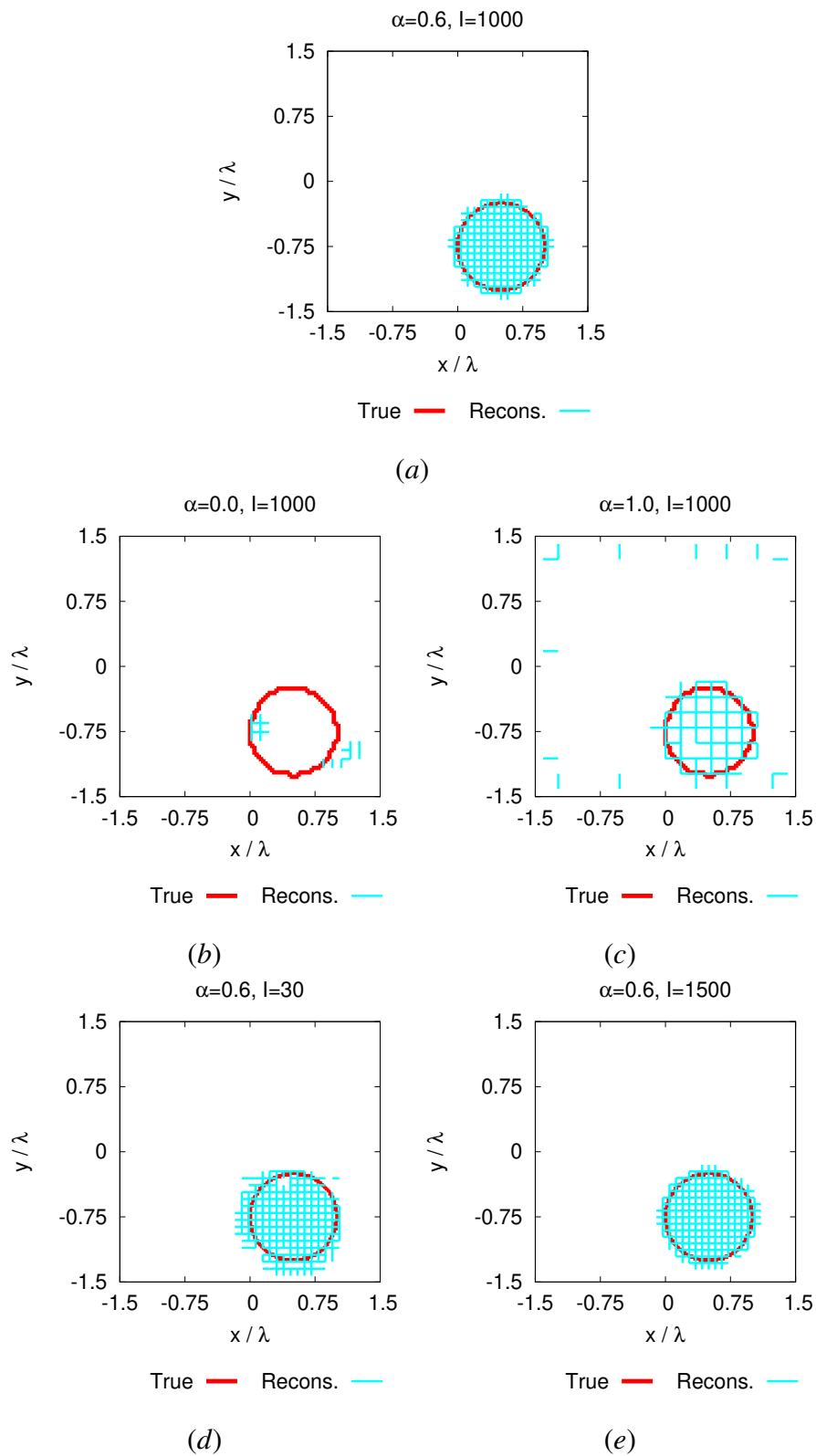


Fig. 5 - Ye et al., “Multi-Resolution Subspace-Based ...”

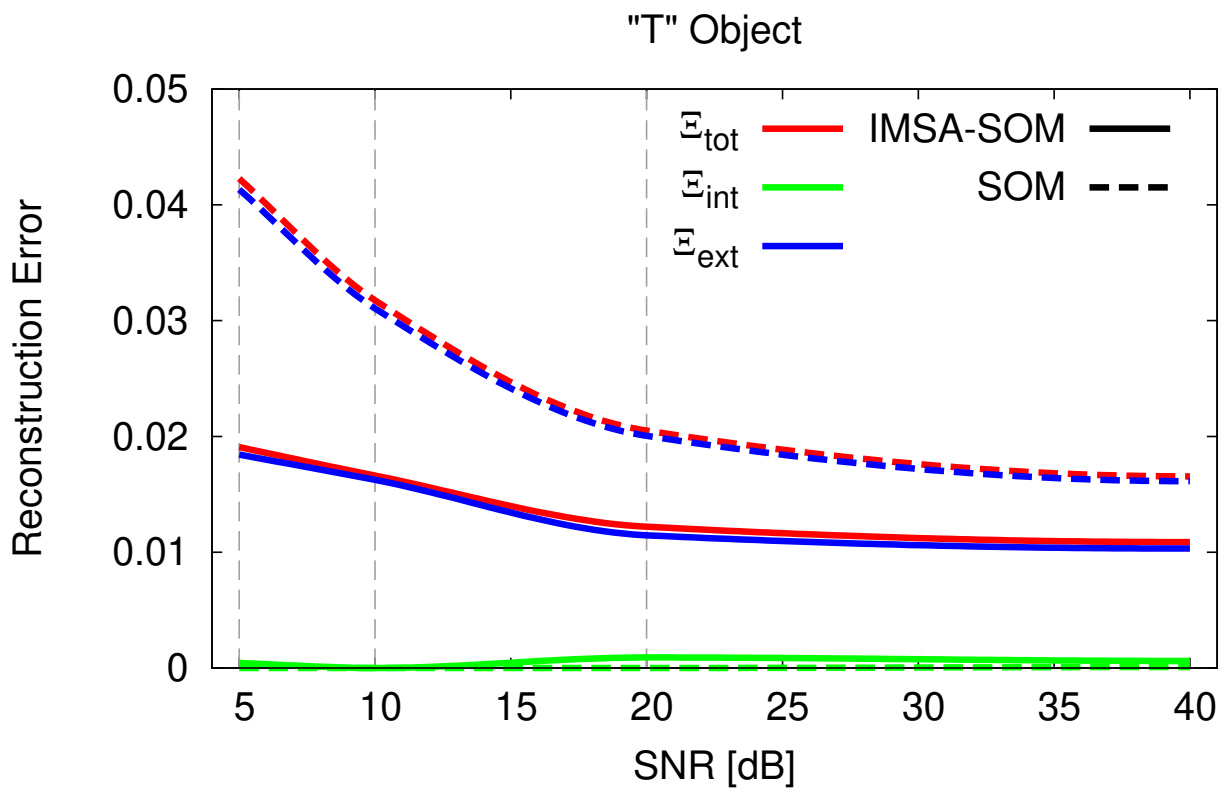


Fig. 6 - Ye et al., "Multi-Resolution Subspace-Based ..."

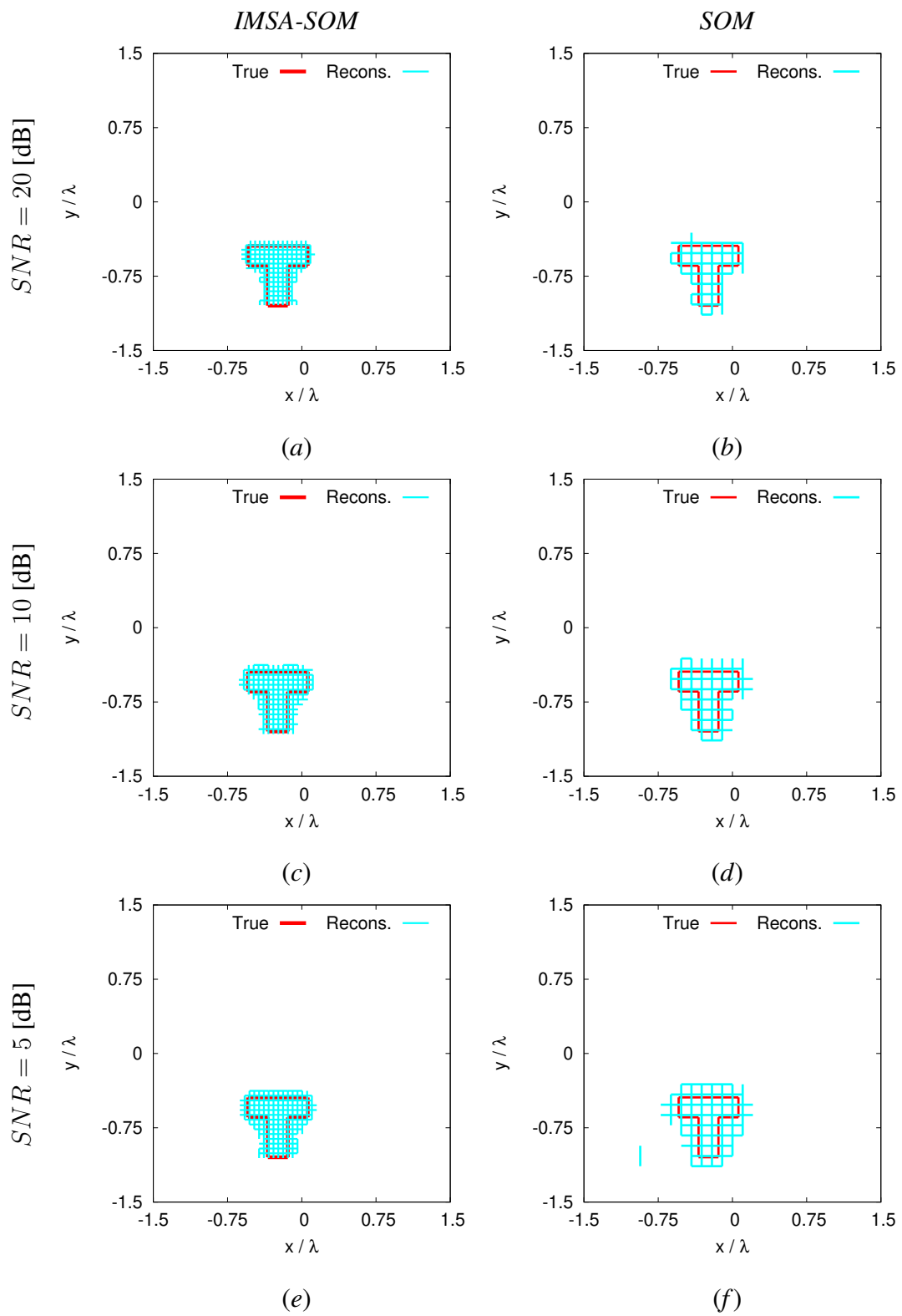


Fig. 7 - Ye et al., “Multi-Resolution Subspace-Based ...”

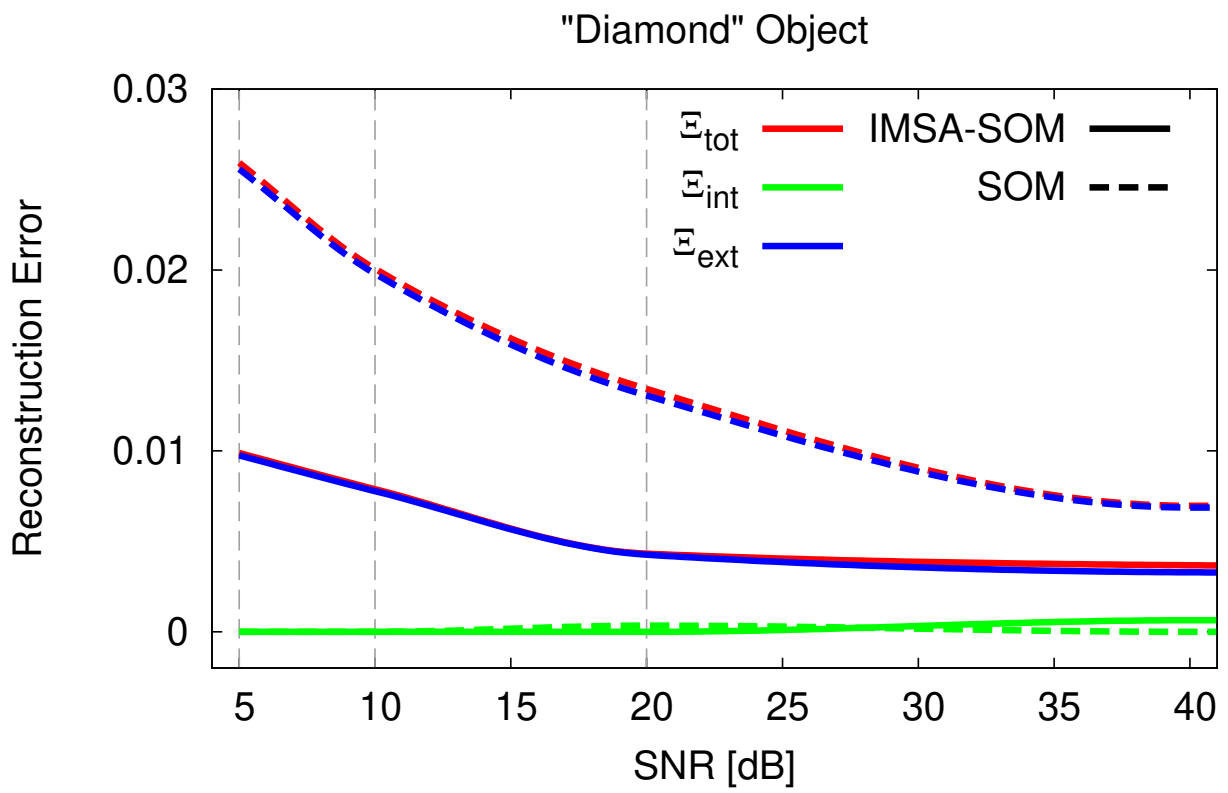


Fig. 8 - Ye et al., "Multi-Resolution Subspace-Based ..."

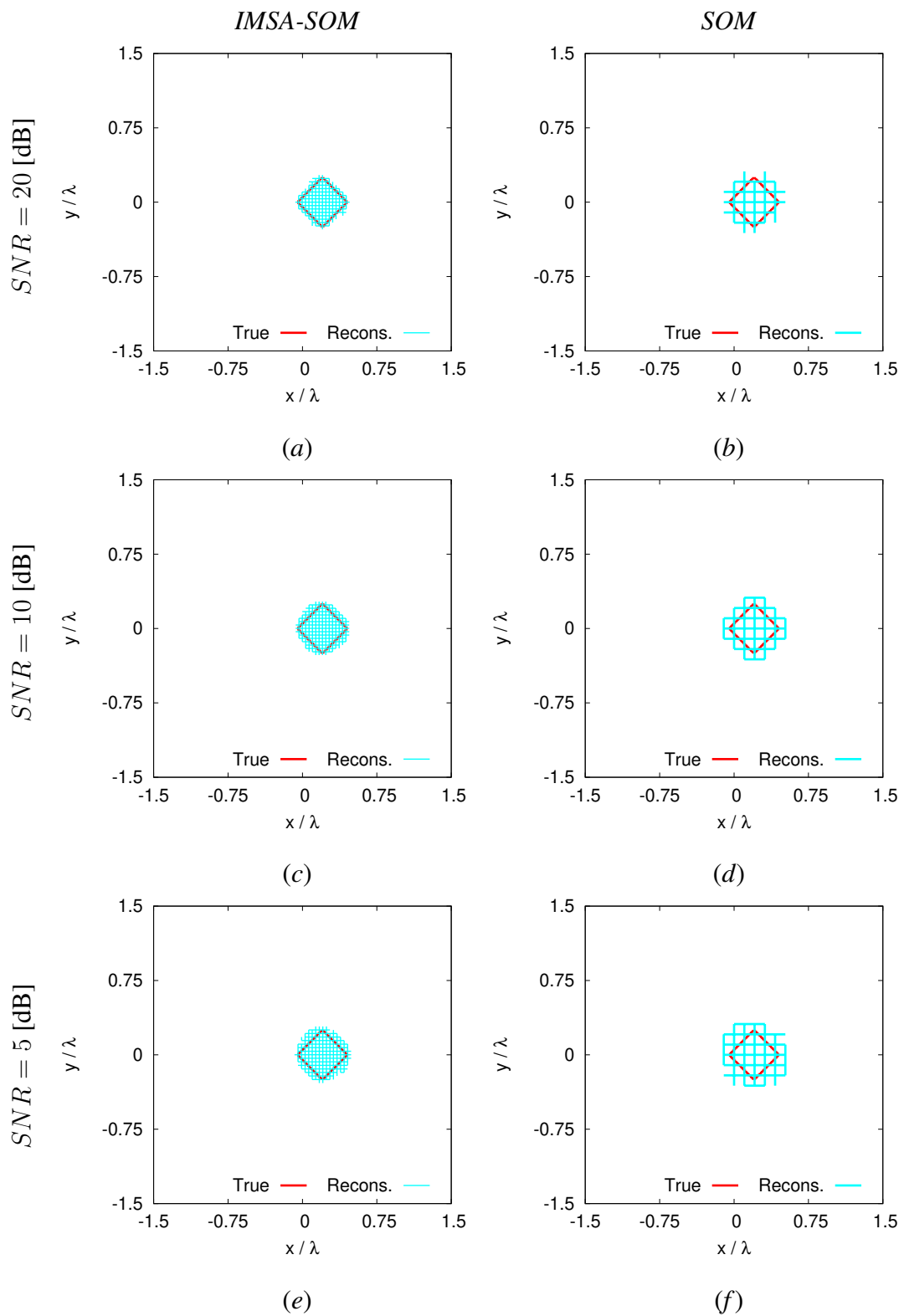


Fig. 9 - Ye et al., “Multi-Resolution Subspace-Based ...”

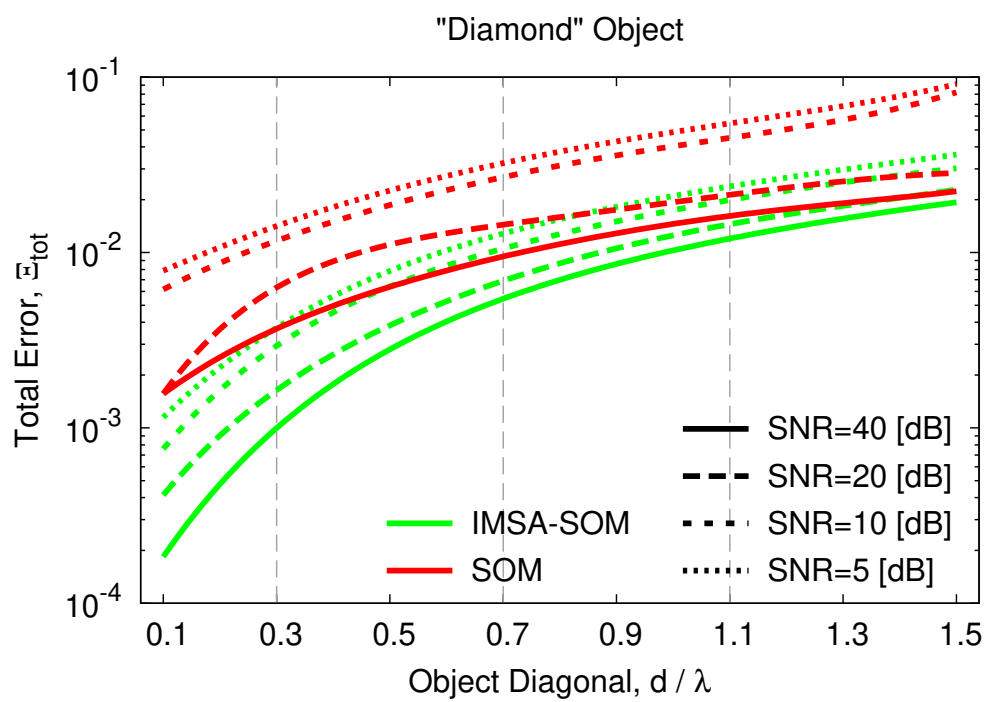


Fig. 10 - Ye et al., "Multi-Resolution Subspace-Based ..."

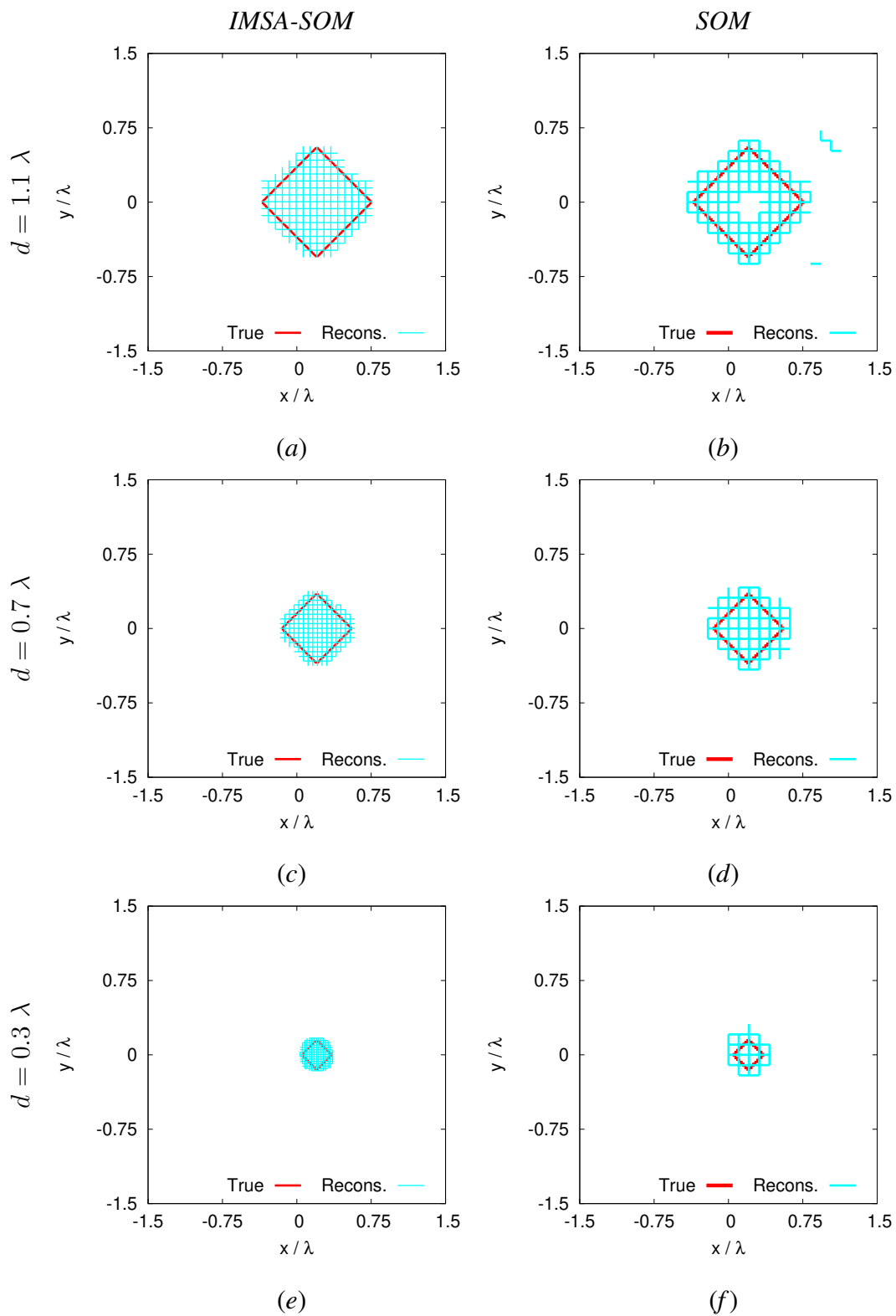


Fig. 11 - Ye et al., “Multi-Resolution Subspace-Based ...”

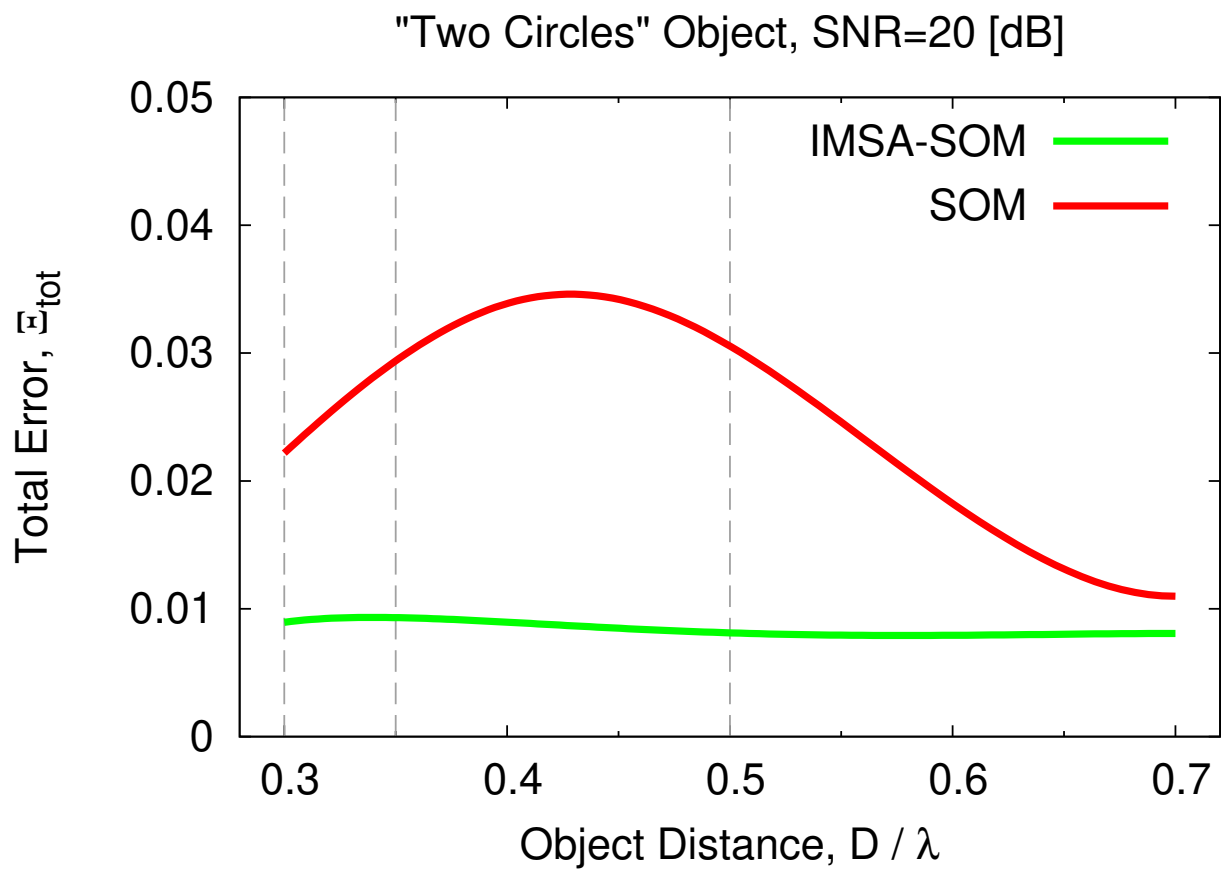


Fig. 12 - Ye *et al.*, "Multi-Resolution Subspace-Based ..."

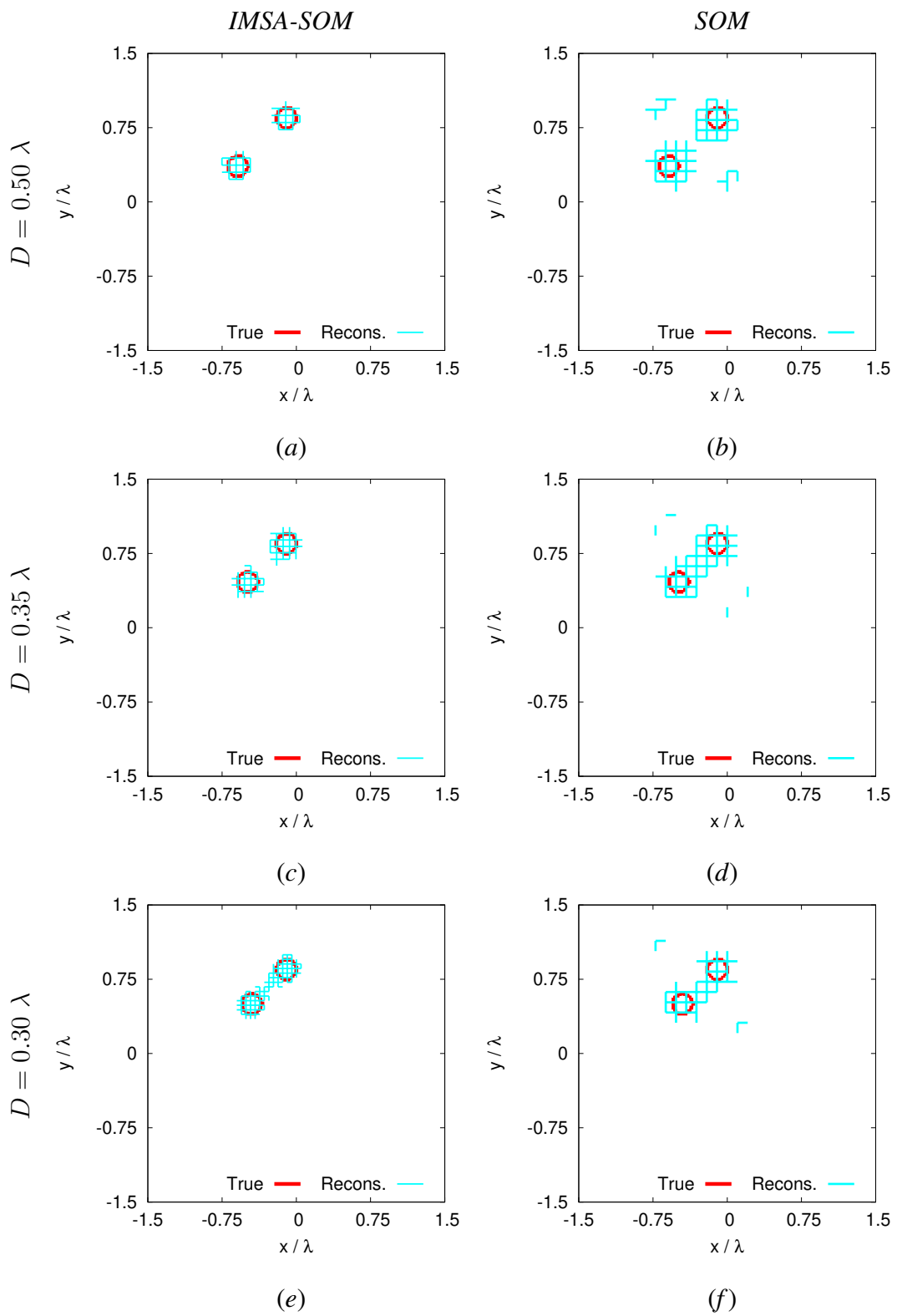


Fig. 13 - Ye et al., “Multi-Resolution Subspace-Based ...”

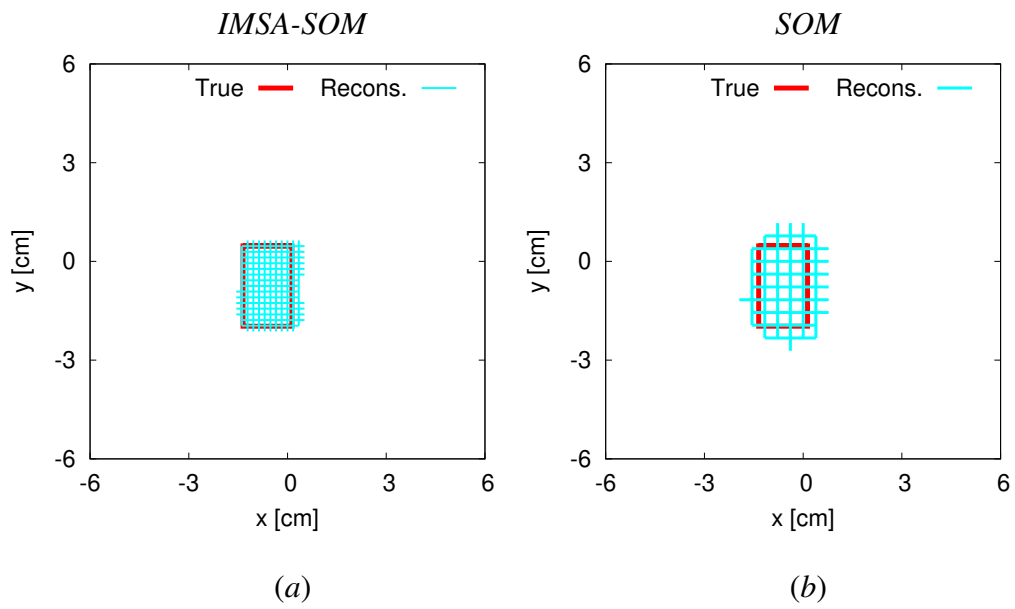


Fig. 14 - Ye et al., “Multi-Resolution Subspace-Based ...”

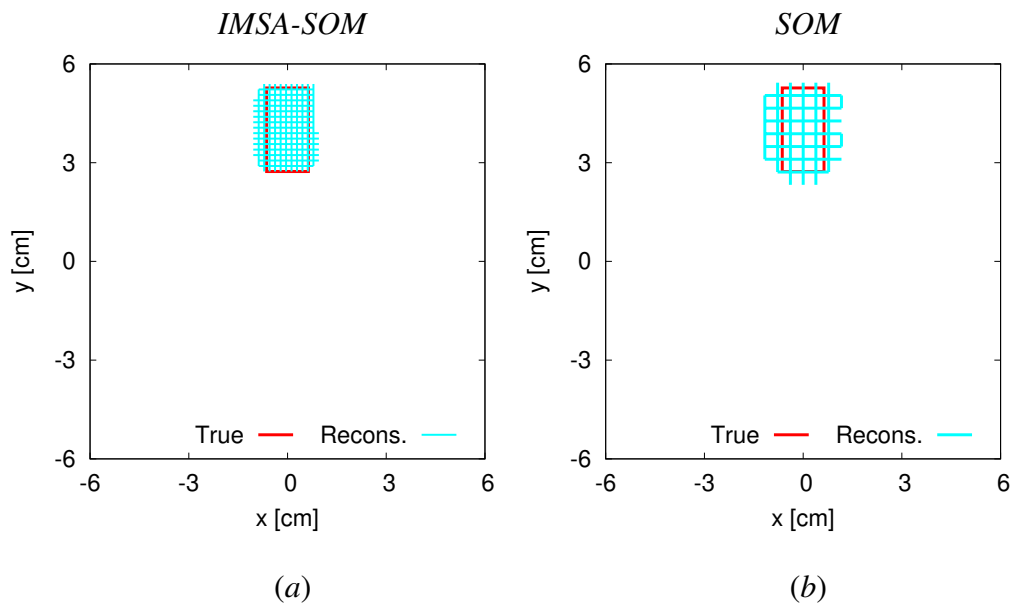


Fig. 15 - Ye et al., “Multi-Resolution Subspace-Based ...”

	$\Xi_{tot} [\times 10^{-2}]$		\mathcal{T} [min]	
	<i>IMSA-SOM</i>	<i>BARE-SOM</i>	<i>IMSA-SOM</i>	<i>BARE-SOM</i>
“rectTM_cent”	1.67	3.71	124	550
“rectTM_dece”	1.39	2.80	120	430

Tab. I - Ye et al., “Multi-Resolution Subspace-Based ...”